

Article

Order-Aware Uncertainty Minimization Network for Fast High Angular Resolution Diffusion Imaging with Unpaired Data

Yunlong Gu ¹, Ying Cao ¹, Li Wang ¹, Qijian Chen ¹ and Yuemin Zhu ^{2,*}

¹ Engineering Research Center of Text Computing and Cognitive Intelligence, Ministry of Education, Key Laboratory of Intelligent Medical Image Analysis and Precise Diagnosis of Guizhou Province, State Key Laboratory of Public Big Data, College of Computer Science and Technology, Guizhou University, Guiyang 550025, China

² CREATIS, CNRS UMR 5220, Inserm U1294, INSA Lyon, University of Lyon, 69007 Lyon, France

* Correspondence: yue-min.zhu@creatis.insa-lyon.fr

Abstract: Diffusion magnetic resonance imaging (dMRI) is an indispensable technique in today's neurological research, but its signal acquisition time is extremely long due to the need to acquire signals in multiple diffusion gradient directions. Supervised deep learning methods often require large amounts of complete data to support training, whereas dMRI data are difficult to obtain. We propose a deep learning model for the fast reconstruction of high angular resolution diffusion imaging in data-unpaired scenarios. Firstly, two convolutional neural networks were designed for the recovery of k-space and q-space signals, while training with unpaired data was achieved by reducing the uncertainty of the prediction results of different reconstruction orders. Then, we enabled the model to handle noisy data by using graph framelet transform. To evaluate the performance of our model, we conducted detailed comparative experiments using the public dataset from human connectome projects and compared it with various state-of-the-art methods. To demonstrate the effectiveness of each module of our model, we also conducted reasonable ablation experiments. The final results showed that our model has high efficiency and superior reconstruction performance.

Keywords: diffusion magnetic resonance imaging; high angular resolution diffusion imaging; deep learning; compressed sensing; brain imaging



Citation: Gu, Y.; Cao, Y.; Wang, L.; Chen, Q.; Zhu, Y. Order-Aware Uncertainty Minimization Network for Fast High Angular Resolution Diffusion Imaging with Unpaired Data. *Electronics* **2023**, *12*, 2985. <https://doi.org/10.3390/electronics12132985>

Academic Editor: Heung-Il Suk

Received: 18 May 2023

Revised: 2 July 2023

Accepted: 3 July 2023

Published: 6 July 2023



Copyright: © 2023 by the authors. Licensee MDPI, Basel, Switzerland. This article is an open access article distributed under the terms and conditions of the Creative Commons Attribution (CC BY) license (<https://creativecommons.org/licenses/by/4.0/>).

1. Introduction

Currently, diffusion magnetic resonance imaging (dMRI) is one of the noninvasive and radiation-free technique for detecting changes in human tissues. By collecting at least six diffusion-weighted images (DWIs) from different directions and using a least-squares fitting method to estimate the diffusion tensor image (DTI), dMRI can measure water molecule diffusion in tissues and reconstruct tissue fiber orientation, reflecting the microstructure of tissues. In recent years, DTI has been widely used as an auxiliary diagnostic tool for diseases such as Parkinson's disease, depression, and Alzheimer's disease. However, because DTI assumes that water molecule displacement in tissues follows a Gaussian distribution, it cannot accurately reflect complex fiber structures such as fiber crossings.

To accurately estimate complex fiber structures from data, high angular resolution diffusion imaging (HARDI) utilizes techniques such as spherical harmonic transformation to estimate multiple crossing fiber directions. Although HARDI provides an effective means of detecting complex fiber structures, this is achieved by collecting a minimum of 50 diffusion-weighted images in various directions and results in long acquisition times that limit clinical applications. Therefore, shortening the HARDI acquisition time while maintaining image quality is crucial for the accurate estimation of complex tissue fiber structures and assisting clinical diagnosis.

Currently, there are two main strategies for shortening the HARDI acquisition time. The first strategy involves improving hardware efficiency through parallel imaging tech-

niques such as simultaneous acquisition of spatial harmonics (SMASH) [1] and sensitivity encoding (SENSE) [2]. These methods use multiple coils to acquire signals in parallel, which are then combined to reconstruct the complete signal. However, these hardware-based methods have limitations in terms of the acceleration level and can introduce more noise and overlapping artifacts.

The second strategy involves reducing the number of acquired signals and using algorithms to recover the complete signal from a small amount of data. One representative method is based on compressed sensing (CS) [3,4], which exploits the sparsity or low-rank properties of signals to reconstruct k-space data efficiently. Here, k-space refers to the frequency domain in which magnetic resonance imaging (MRI) data are collected. Traditional CS reconstruction often uses iterative optimization algorithms that are slow [5,6]. With convolutional neural networks (CNN) [7] impressing in the field of computer vision [8–10], ADMM-net [11] used a cascaded network structure based on the alternating direction method of multipliers (ADMM) [12], which incorporates convex optimization problem decomposition and subproblem parallelization into deep learning models to improve speed. Similarly, the ISTA-net and ISTA-net+ [13] models use the iterative shrinkage threshold algorithm [14], along with the soft-thresholding iteration structure and sparse prior, to enhance signal reconstruction efficiency in convolutional neural networks. The CRNN [15] model integrates convolutional recurrent neural networks with traditional iterative algorithms to accelerate the reconstruction process. Instead of relying on the iterative approach of conventional algorithms, CRNN employs forward propagation of convolutional recurrent neural networks for faster and more efficient reconstruction.

However, these methods still rely on traditional priors that may limit their performance in texture detail enhancement tasks. The DAGAN [16] model combines U-Net [17] with generative adversarial networks to remove artifacts and refine the details of MRI images effectively. RefineGAN [18] utilizes deeper generators and discriminators with cycle consistency loss for better artifact removal and detail recovery. KIKI-net [19] performs convolution operations alternately between the k-space domain and spatial domain while exchanging information between them iteratively. MdRecon-Net [20] extracts and fuses k-space and image features separately using two shared network branches for improved signal recovery results. Overall, these studies demonstrate how deep learning techniques can significantly accelerate the computation speed of traditional iterative optimization algorithms while enhancing MRI image quality by exploiting both frequency-domain information from k-space data and spatial-domain information from DWIs simultaneously.

Compared to MRI data, dMRI data are sparse not only in k-space but also in q-space, which is a term used in dMRI to describe the domain in which the diffusion data are represented. Therefore, some researchers have undersampled signals in q-space and reconstructed the original q-space data using compressed sensing algorithms. For instance, Koppers et al. developed a fully connected network model that utilized single-shell HARDI data to generate multishell HARDI data, thereby improving the acquisition speed of HARDI [21]. However, their approach did not consider the spatial relationship between voxels leading to suboptimal reconstruction results. In contrast, Jha et al. considered both the spatial position relationship between voxels and the relationship between different directional signals within voxels by generating multidirectional DWIs from few-direction DWIs and further improved the compressed sensing reconstruction effect of DWIs [22]. RCNN [23] directly utilizes LSTM to build an encoder–decoder with 3D convolution to learn the relationship between the spatial domain and q-space. SPC-GAAN [24] uses 3D convolution to reconstruct dMRI data in both the spatial domain and k-space, while introducing adversarial learning strategies and attention mechanisms to make the reconstructed dMRI data closer to real data. However, this method requires a large amount of memory space and has certain requirements for data size. Performing k-space and q-space undersampling simultaneously while reconstructing the original complete signal can significantly accelerate HARDI imaging speed. Vaish et al. proposed MSR-HARDI [25] for joint k-q space reconstruction of dMRI using the Smooth-FISTA method based on multiple

sparse regularization terms for signal recovery, which proved feasible for the joint k-q space reconstruction method. On the other hand, Mani et al. trained a denoiser using deep learning as a regularization term for joint k-q space reconstruction providing an idea for deep learning-based k-q space reconstruction methods [26].

Although the above-mentioned methods have achieved fast and accurate reconstruction of HARDI, they still require a large amount of fully sampled HARDI images as labels for training, which has certain limitations in clinical applications. To address this issue, a self-supervised deep learning reconstruction model was proposed using compressed sensing and the concept of SSDU [27]. It performs division on undersampled k-space signals, predicts missing signals based on the available part signals, and achieves label-free data reconstruction. This demonstrates the feasibility of self-supervised MRI compressed sensing reconstruction. Cole et al. combined self-supervised strategies with adversarial generative networks and designed an unpaired k-space signal reconstruction method using adversarial learning, expanding the idea of self-supervised compressed sensing reconstruction [28]. However, existing self-supervised models focus only on accelerated k-space reconstruction and it is difficult to further improve HARDI imaging speed without considering q-space information. Reconstructing the HARDI signal in k-q space using limited data remains a challenging task.

In this paper, we propose an unpaired HARDI reconstruction network based on minimizing the uncertainty of reconstruction order, aiming to jointly utilize k-q space information and achieve the high-quality reconstruction of HARDI signals in cases where some labels are not paired. The main contributions are as follows:

- (1) We designed a cascaded model for jointly compressed sensing reconstruction of HARDI data in both k-space and q-space. The model consists of two parts: the k-space reconstruction model and the q-space reconstruction model. The former obtains effective neighborhood information from both the image domain and Fourier domain to supplement the undersampled signal, while the latter obtains highly correlated information from both the image domain and q-space domain, ensuring high-quality images at lower sampling rates;
- (2) Considering that the order of disrupting k-space reconstruction and q-space reconstruction will affect the reconstruction effect of the model and increase the uncertainty of the reconstruction results, a training strategy was designed to reduce the uncertainty of predicting different reconstruction orders, which can ensure the reconstruction effect of the model under conditions where some data are not paired;
- (3) To reduce the impact of noise on the model reconstruction performance, we introduced a graph framelet transform (GFT)-based denoising module that enhances the robustness of the model.

2. Materials and Methods

HARDI requires scanning of DWIs with multiple b-values and directions, which together form q-space. Here, b-value is a parameter used in DWI to quantify the extent of diffusion weighting applied to the MRI signal. The corresponding DWI is obtained by acquiring k-space signals and performing Fourier transform when given a direction and b-value. To reduce the acquisition time of HARDI, sampling is typically performed on either k-space or q-space (as shown in Figure 1A,B). We propose a joint k-q space sampling strategy (Figure 1C) to further improve the sampling rate while enhancing the reconstruction quality of HARDI, named the order-aware uncertainty minimization (OAUM) network.

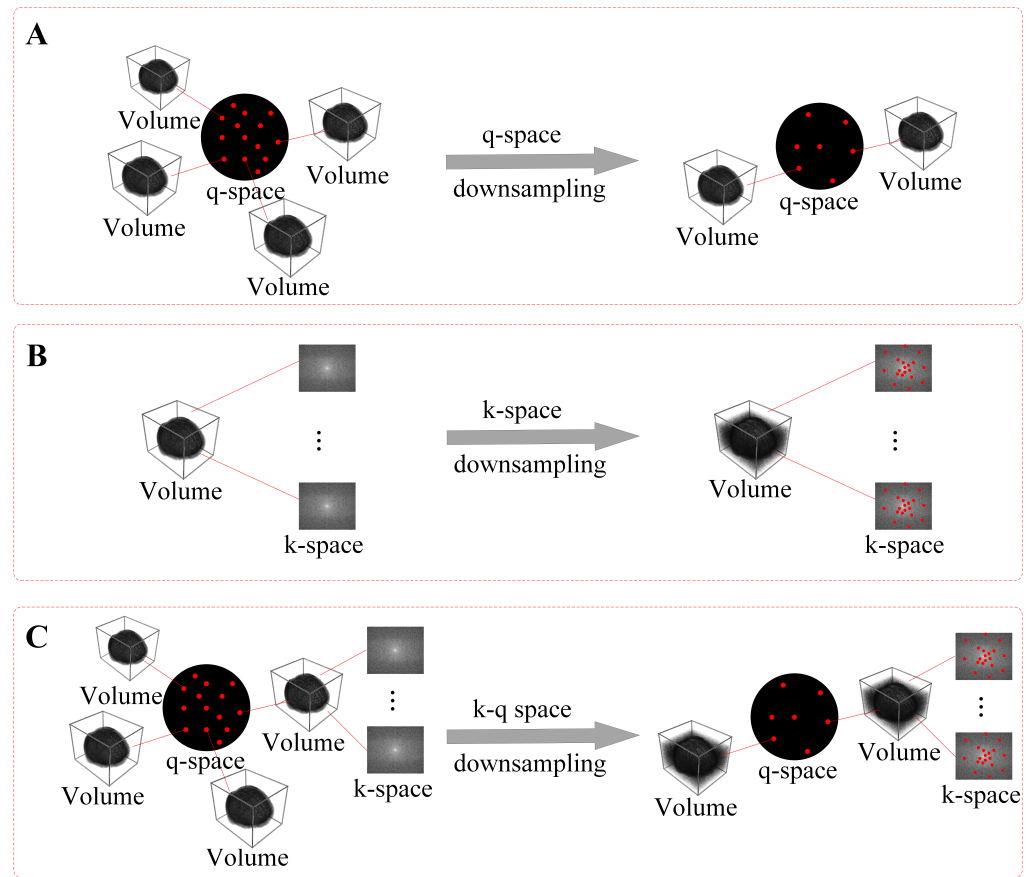


Figure 1. Sampling patterns: (A) only sampling in k-space; (B) only sampling in q-space; (C) jointly sampling in k-q space.

Jointly sampling in k-q space can effectively reduce the acquisition time of HARDI. However, the order of reconstructing k-space and q-space affects the reconstruction quality of HARDI, leading to increased uncertainty in the results. Ideally, HARDI results obtained through different reconstruction orders should be consistent. To address this issue, we propose a reconstruction model that enforces consistency to improve training on unpaired samples. For ease of reference, we denote the DWI slice with full sampling in k-q space as $\mathbf{s}_{f,f} = \{\mathbf{x}_f^i; i = 1, \dots, n\}$, where $\mathbf{x}_f^i \in \mathbb{R}^2$ denotes a k-space fully sampled 2D slice in direction i and n denotes the number of directions. The subscript f here represents the full sampling, and u the undersampling. The first subscript indicates whether k-space is undersampled, and the second subscript means whether q-space is undersampled. Undersampled data in q-space are denoted as $\mathbf{s}_{f,u} = \{\mathbf{x}_f^i; i \in \mathbf{m}^q\}$ where $\mathbf{m}^q = \{j; 1 \leq j \leq n\}$ denotes the undersampling mask in q-space. Undersampled data in k-space are denoted as $\mathbf{s}_{u,f} = \{\mathbf{x}_u^i; i = 1, \dots, n\}$ where \mathbf{x}_u^i denotes a k-space undersampled 2D slice in direction i . DWI data simultaneously undersampled in both k-space and q-space as $\mathbf{s}_{u,u} = \{\mathbf{x}_u^i; i \in \mathbf{m}^q\}$. Our unpaired training dataset consists of two parts: $\mathbf{s}_{f,u_1} = \{\mathbf{s}_f^i; i \in \mathbf{m}_1^q\}$ and $\mathbf{s}_{u,u_2} = \{\mathbf{x}_u^i; i \in \mathbf{m}_2^q\}$ where $\mathbf{m}_1^q \cap \mathbf{m}_2^q = \emptyset$ and $\mathbf{m}_1^q \cup \mathbf{m}_2^q = \{1, \dots, n\}$. The task of reconstructing k-space and q-space involves solving the mapping relationship between undersampled data and fully sampled data. Therefore, their formalized reconstruction processes are given below:

$$\hat{\mathbf{s}}_{f,f}^{k \rightarrow q} = \mathbf{h}_q(\hat{\mathbf{s}}_{f,u}; \theta_q) = \mathbf{h}_q(\mathbf{h}_k(\mathbf{s}_{u,u}; \theta_k); \theta_q) = \mathbf{h}_q(\{\mathbf{h}_k(\mathbf{x}_u^i; \theta_k); i \in \mathbf{m}_q\}; \theta_q) \quad (1)$$

$$\hat{\mathbf{s}}_{f,f}^{q \rightarrow k} = \mathbf{h}_k(\hat{\mathbf{s}}_{u,f}; \theta_k) = \mathbf{h}_k(\mathbf{h}_q(\mathbf{s}_{u,u}; \theta_q); \theta_k) = \{\mathbf{h}_k(\hat{\mathbf{x}}_u^i; \theta_k); i = 1, \dots, n\} \quad (2)$$

Equation (1) defines $h_k(\cdot; \theta_k)$ as the reconstruction mapping function in k-space, where θ_k represents the network parameters for k-space reconstruction. Similarly, $h_q(\cdot; \theta_q)$ represents the reconstruction mapping function in q-space and its corresponding mapping parameters. In addition, $\hat{\mathbf{s}}_{f,f}$ designates the HARDI data jointly reconstructed from k-q space. $\hat{\mathbf{x}}_u^i$ denotes the q-space data reconstructed from undersampled k-space. Ideally, different orders of reconstruction should yield identical results:

$$\hat{\mathbf{s}}_{f,f} = \hat{\mathbf{s}}_{f,f}^{q \rightarrow k} = \hat{\mathbf{s}}_{f,f}^{k \rightarrow q} \quad (3)$$

However, during the predicting process, prediction errors can cause overlapping and interference between reconstruction errors in k-space and q-space. The order of reconstruction may also introduce uncertain perturbations to the results. To improve the stability and effectiveness of DWI reconstruction, it is necessary to reduce uncertainty related to order of reconstruction. We propose a consistency constraint for different orders of k-space and q-space reconstructions:

$$\arg \min_{\theta_k, \theta_q} \|h_{k \rightarrow q}(\mathbf{s}_{u,u}; \theta_k, \theta_q) - h_{q \rightarrow k}(\mathbf{s}_{u,u}; \theta_k, \theta_q)\|_2^2 \quad (4)$$

The model framework shown in Figure 2 includes $h_{k \rightarrow q}(\mathbf{s}_{u,u}; \theta_k, \theta_q)$ and $h_{q \rightarrow k}(\mathbf{s}_{u,u}; \theta_k, \theta_q)$, which represent the reconstruction of the k-space signal followed by the reconstruction of the q-space signal and the reconstruction of the q-space signal followed by the reconstruction of the k-space signal. In addition, the network shares the parameters of the identical module.

To begin, the k-q space jointly undersampled data $\mathbf{s}_{u,u}$ must be inputted into parallel reconstruction networks for both k-space and q-space. This will result in the preliminary restoration of the data, producing $\hat{\mathbf{s}}_{f,u}$ and $\hat{\mathbf{s}}_{u,f}$. Once this step is complete, these results are then alternately fed back into opposite reconstruction modules to obtain the final reconstructed output. The subsequent section will provide a comprehensive description of the k-space and q-space reconstruction networks used in this process.

2.1. k-Space Reconstruction Module

The DWI resulting from the undersampled k-space signal in any gradient direction can be expressed as:

$$\mathbf{x}_u = \mathcal{F}^{-1}(\mathbf{m}^k \mathcal{F}(\mathbf{x}_f)) \quad (5)$$

The following notations are used: $\mathcal{F}(\cdot)$ for Fourier transform, $\mathcal{F}^{-1}(\cdot)$ for inverse Fourier transform, and $\mathbf{m}^k \in \mathbb{R}^2$ for a random sampling matrix. Thus, the objective of optimizing k-space reconstruction is:

$$\arg \min_{\theta_k} \|h_k(\mathbf{x}_u; \theta_k) - \mathbf{x}_f\|_2^2 \quad (6)$$

Figure 2B shows the model structure of $h_k(\cdot; \theta_k)$. Before inputting data into the model, it is necessary to adjust the data dimension. The original input data size is (B, D, H, W) , where B represents batch size, D the number of directions in DW images, and H and W the height and width of DW images, respectively. To rearrange this data for processing, we convert them into $(B \times D, 1, H, W)$. After Fourier transform, the k-space signal is obtained and represented by two channels for the real and imaginary parts of the signal. These signals are then fed into a stacked deblurring module that produces a so-called k-space completion image. The structure of the deblurring module can be seen as a black box in Figure 2B. Since brain structures have a certain symmetry on the spatial level and k-space signals also have certain symmetry relative to a low-frequency center, we introduce the spatial flip concatenation (SFC) operation (Figure 2D) and k-space flip concatenation (KFC) operation (Figure 2E) in this module. SFC flips along the H direction center for the input

spatial image, while KFC flips along the H and W direction center for the input k-space image. These flipped images are merged before being passed through feature extraction modules that use similar structure assistance features for effective feature extraction. In this way, undersampled images processed by SFC and feature extraction modules can preliminarily remove artifacts. Fourier transform results are transferred to k-space where similar signal restoration can be assisted through KFC combined with feature extraction modules. Finally, the k-space DC layer increases the sensitivity of model reconstruction for missing signal areas. The k-space data consistency layer can be written as KDC:

$$F_{(i,j)}^{out} = \begin{cases} F_{(i,j)}^{in}, & m_{(i,j)}^k = 0 \\ \frac{F(x_u)_{(i,j)} + \alpha F_{(i,j)}^{in}}{1 + \alpha}, & m_{(i,j)}^k = 1 \end{cases} \quad (7)$$

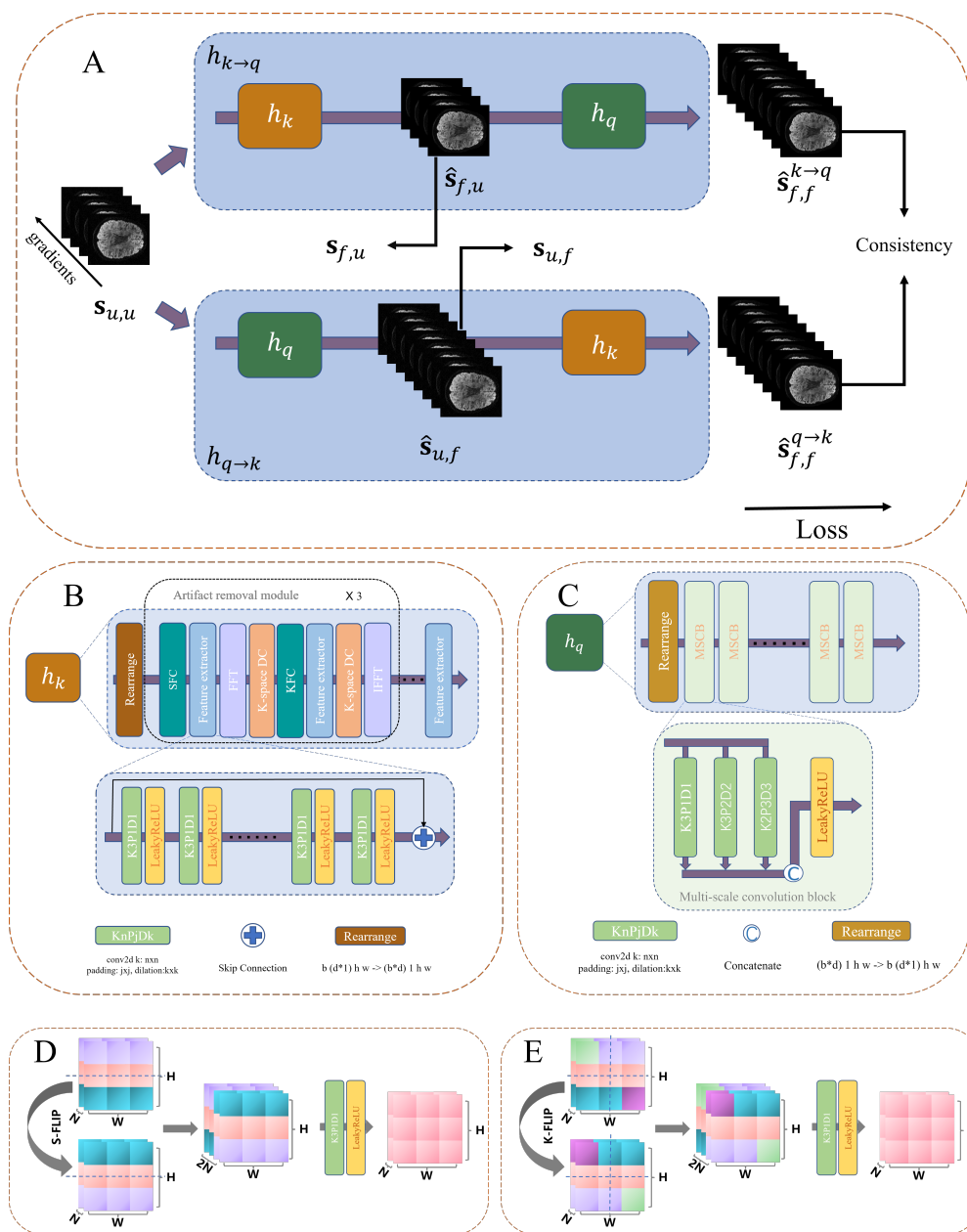


Figure 2. Structure of the proposed OAUM network: (A) schematic diagram of the overall reconstruction process of the network; (B) k-space reconstruction module; (C) q-space reconstruction module; (D,E) the SFC module and the KFC module, respectively, which are used to fuse the symmetrical features of the spatial feature map and the frequency domain feature map.

The variable (i, j) denotes the row and column index of the 2D matrix. The k-space undersampling mask $\mathbf{m}_{(i,j)}^k = 0$ means that the k-space signal is not sampled while $\mathbf{m}_{(i,j)}^k = 1$, which, in turn, means that the k-space signal is sampled at row i and column j . $\mathcal{F}(\mathbf{x}_u)_{(i,j)}$ designates the k-space signal of the original undersampled image at row i and column j . The output restored images' k-space signals from consistency module are represented by $\mathbf{F}_{(i,j)}^{out}$. A tuning parameter α is used to adjust proportion between original signals and restored signals. After being constrained in the frequency domain by the consistency module, inverse Fourier transform can be applied to obtain reconstructed images without aliasing artifacts. Finally, we apply a residual network structure composed of convolutional layers with the LeakyReLU activation function to further refine the reconstruction results. The network can achieve improved restoration of image details by integrating spatial domain antialiasing processing with frequency domain consistency constraints.

2.2. q-Space Reconstruction Module

The total acquisition time is significantly influenced by the number of acquisition directions. In the HARDI model, collecting DWI data with multiple b-values and directions is necessary for estimating crossing fibers. Therefore, q-space reconstruction aims to recover the original multidirectional q-space information from q-space undersampled data to improve the accuracy of fiber crossing estimation. This objective can be compared to k-space undersampling and expressed as follows:

$$\arg \min_{\theta_q} \|\mathbf{h}_q(\mathbf{s}_{.,u}; \theta_q) - \mathbf{s}_{.,f}\|_2^2 \quad (8)$$

where $\mathbf{s}_{.,u}$ and $\mathbf{s}_{.,f}$ represent the undersampled and fully sampled HARDI data in q-space, respectively, while the k-space signal can either be complete or undersampled. Figure 2C shows the model structure of $\mathbf{h}_q(\cdot; \theta_q)$. To capture the correlations of signals at different scales and directions, we use a multiscale convolution module (MSCB) for feature extraction and the reconstruction of q-space images. This module comprises three parallel convolutional layers and one LeakyReLU activation function. Each layer uses dilated convolutions with different dilation factors to convolve the data, resulting in feature maps that are merged on channels before being activated by LeakyReLU. CNN models usually represent different features of data through different channels. Therefore, our q-space reconstruction model assigns DWIs with various gradient directions to corresponding channels precisely. In this way, 2D networks can process 3D data while reducing computational costs without sacrificing reconstruction quality.

2.3. Loss Function

The loss function of this model comprises three components: k-space reconstruction loss, q-space reconstruction loss, and order-independent reconstruction consistency loss. Equation (9) defines the k-space loss:

$$l_k = \|\hat{\mathbf{s}}_{f,u} - \mathbf{s}_{f,u}\|_2^2 = \|\mathbf{h}_k(\mathbf{s}_{u,u}) - \mathbf{s}_{f,u}\|_2^2 \quad (9)$$

where $\hat{\mathbf{s}}_{f,u} = \mathbf{h}_k(\mathbf{s}_{u,u})$ represents the intermediate result obtained through k-space reconstruction model. $\mathbf{s}_{f,u}$ denotes the uncompleted HARDI data in q-space with the fully sampled signal in k-space. The reconstruction loss of q-space can be expressed in a similar manner:

$$l_q = \|\hat{\mathbf{s}}_{u,f} - \mathbf{s}_{u,f}\|_2^2 = \|\mathbf{h}_q(\mathbf{s}_{u,u}) - \mathbf{s}_{u,f}\|_2^2 \quad (10)$$

where $\hat{\mathbf{s}}_{u,f} = \mathbf{h}_q(\mathbf{s}_{u,u})$ denotes k-space undersampled DWIs that have been reconstructed and completed in q-space. $\mathbf{s}_{u,f}$ represents the k-space undersampled DWIs that have been fully sampled in q-space. This loss function helps to ensure the accurate directional reconstruction.

In addition, to ensure that the DW images obtained under different reconstruction orders are consistent, we introduce a loss function for order-independent reconstruction consistency. The expression is as follows:

$$l_c = \|\mathbf{h}_k(\mathbf{h}_q(\mathbf{s}_{u,u})) - \mathbf{h}_q(\mathbf{h}_k(\mathbf{s}_{u,u}))\|_2^2 = \|\mathbf{h}_k(\hat{\mathbf{s}}_{u,f}) - \mathbf{h}_q(\hat{\mathbf{s}}_{f,u})\|_2^2 \tag{11}$$

The lost signal in k-space can be reconstructed either before completing q-space data or after. Both methods should yield the same result. Therefore, the loss function of the network is:

$$l = \lambda_1 l_k + \lambda_2 l_q + \lambda_3 l_c \tag{12}$$

where λ_1 , λ_2 , and λ_3 are hyperparameters that control the weights of three loss functions.

2.4. Reconstruction of Noisy HARDI Data Using Graph Framelet Transforms

The OAUM technique is proficient in rapidly and efficiently reconstructing noise-free HARDI data. However, obtaining such data in clinical settings can be challenging. To address this issue, we develop here a module that utilizes OAUM to swiftly denoise q-space signals. This module initially represents the input noisy q-space signal as a graph and then applies graph framelet transform (GFT) to segregate various frequency bands of the graph signal [29]. By selecting appropriate levels and frequency bands, we obtain nearly noise-free HARDI data, which are subsequently fed into the OAUM network for reconstruction. The outcome is a reconstructed image that is almost free from any noise. This method is referred to as the denoised-OAUM(DN-OAUM).

2.4.1. Graph Representation of q-Space

To begin, we consider every point in the q-space as a vertex on a graph. We then determine the correlation between each pair of points by utilizing their b-values and gradient direction vectors as weights for the edges. To represent the weight between two points i and i' in q-space, we use $a_{i,i'}$. The values of i and i' range from 1 to n , where n is the maximum number of gradient directions in the data. The calculation method for determining these weights is as follows:

$$a_{i,i'} = \exp\left(-\frac{1 - (\bar{\mathbf{q}}_i^T \bar{\mathbf{q}}_{i'})^2}{2\sigma_q^2}\right) \exp\left(-\frac{(\sqrt{b_i} - \sqrt{b_{i'}})^2}{2\sigma_b^2}\right) \tag{13}$$

The given formula utilizes various variables to calculate the adjacency matrix A for a graph. Specifically, $\bar{\mathbf{q}}_i = \mathbf{q}_i / \|\mathbf{q}_i\|$ represents the normalized direction vector of point i , while b_i denotes the b value at point i . Additionally, hyperparameters σ_q and σ_b are employed to control the two exponential decays. By applying this formula, we can determine the correlation between each pair of points and obtain a symmetric adjacency matrix $A = \{a_{i,i'}; i = 1, \dots, n; i' = 1, \dots, n\}$ for our graph. Then, we can build a graph $G = \{v, e, w\}$ with vertices represented by $v = \{1, \dots, n\}$, edges denoted by $e \subseteq \{(1, 1), (1, 2), \dots, (n, n)\}$ and weights given by w . If $a_{i,i'} > 0$, then (i, i') is an edge in the graph with weight equal to $a_{i,i'}$. The degree of each vertex can be computed by:

$$d_i = \sum_{i'=1, i' \neq i}^n a_{i,i'} \tag{14}$$

To perform graph framelet transforms, we obtain the degree matrix \mathbf{D} and Laplacian matrix \mathbf{L} of the graph. The degree matrix is obtained by taking the diagonal elements d_i for $i = 1, \dots, n$. The Laplacian matrix is then calculated as $\mathbf{L} = \mathbf{D} - \mathbf{A}$, where \mathbf{A} is the adjacency matrix of the graph. An eigendecomposition on the Laplacian matrix is performed to obtain its eigenvalues and eigenvectors. Denote these as $\{\lambda_i; 0 = \lambda_1 \leq \lambda_2 \leq \dots \lambda_n = \lambda_{max}\}$ and $\mathbf{U} = \{\boldsymbol{\mu}_i\}$, respectively, where λ_{max} is the maximum eigenvalue.

Once we have obtained these matrices, we can proceed with performing graph framelet transforms.

2.4.2. Denoising Using Graph Framelet Transforms

Graph framelet transforms decompose the graph signal to various frequency bands using a set of masks $\{\hat{a}_r(\cdot); r = 0, \dots, R\}$. Each mask is used for filtering signals in different frequency bands, where $\hat{a}_0(\cdot)$ is utilized for low-pass filtering. The GFT of noisy signals defined on the graph, denoted as $\check{\mathbf{s}}$, can be written as:

$$\boldsymbol{\alpha} = \mathbf{W}\check{\mathbf{s}} = \{\boldsymbol{\alpha}_{l,r} = \mathbf{W}_{l,r}\check{\mathbf{s}}; (l,r) \in B_{L,R}\} \tag{15}$$

where $B_{L,R} = \{(1,1), \dots, (L,R)\} \cup \{(L,0)\}$ and L is the maximum decomposition level. The process of solving \mathbf{W} is as follows:

$$\mathbf{W}_{l,r} = \begin{cases} \mathbf{U}\hat{\Omega}_r(\gamma^{-L+1}\tilde{\Lambda})\mathbf{U}^T & l = 1, \\ \mathbf{U}\hat{\Omega}_r(\gamma^{-L+l}\tilde{\Lambda})\hat{\Omega}_0(\gamma^{-L+l-1}\tilde{\Lambda}) \dots \hat{\Omega}_r(\gamma^{-L+l-1}\tilde{\Lambda})\mathbf{U}^T & 2 \leq l \leq L \end{cases} \tag{16}$$

where $\tilde{\Lambda} = \text{diag}\{\tilde{\lambda}_i; i = 1, \dots, n\}$, $\tilde{\Omega}_r(c\tilde{\Lambda}) = \text{diag}\{\hat{a}_r(c\tilde{\lambda}); i = 1, \dots, n\}$. The present study uses Haar mask, namely, $\hat{a}_0(\tilde{\zeta}) = \cos(\frac{\tilde{\zeta}}{2})$, $\hat{a}_1(\tilde{\zeta}) = \sin(\frac{\tilde{\zeta}}{2})$. We use the low-pass filter operator $W_{1,0}$ to denoise the signal on q-space:

$$\mathbf{s} = \boldsymbol{\alpha}_{1,0} = \mathbf{W}_{1,0}\check{\mathbf{s}} \tag{17}$$

The final result is a noise-free signal \mathbf{s} . The network architecture for denoising using GFT is depicted in Figure 3.

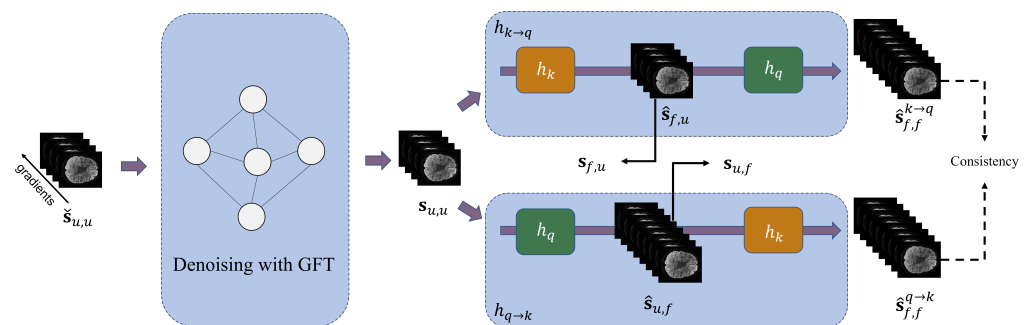


Figure 3. Structure of the proposed DN-OAUM network.

2.5. Dataset and Preprocessing

This work utilizes data from the Human Connectome Project (HCP) public dataset [30], which was acquired using a 3T Siemens MRI machine. All dMRI data were obtained with the same imaging protocol. The diffusion-weighted images were collected on three spherical shells at $b = 1000 \text{ s/mm}^2$, $b = 2000 \text{ s/mm}^2$, and $b = 3000 \text{ s/mm}^2$, with each shell consisting of 90 diffusion gradient directions. The slice thickness was 1.25 mm. Additionally, 18 structural images were obtained at $b = 0$. Consequently, every subject had a total of 270 DWIs and 18 b0 images. Each subject underwent scanning for 145 slices, resulting in a data size of $145 \times 174 \times 145 \times 288$ per individual.

In the experiment of OAUM, we initially randomly selected 13 subjects with brain skull as the dataset. We used 10 subjects for training, 1 subject for validation, and the remaining 2 for testing. Then, we used the Patch2Self [31] method to denoise and preprocess the data to simulate noiseless data. In order to save time during training and verify our reconstruction idea’s feasibility, we only selected the middle 72 slices of each subject’s data for training. We randomly sampled 64 directions of HARDI data from $b = 1000 \text{ s/mm}$ as ground truth for the reconstruction analysis. After downsampling the DWIs at 32 gradient directions using a k-space downsampling template, they were used as labeled data for the unpaired training

dataset of the model. Therefore, during both the model training and testing phases, each subject's data size was $145 \times 174 \times 72 \times 64$ with undersampled k-space on 32 directions. Before inputting into network models, grayscale normalization was performed separately on both the training set and test set.

In the DN-OAUM experiment, all aspects of data processing were consistent with those used in the OAUM experiment, except for the use of noisy HARDI data as the input of the network. In addition, we trained the OAUM network using HARDI data denoised using the Patch2Self and Neighbor2Neighbor [32] methods, for comparison with DN-OAUM.

2.6. Sampling and Model Training Parameter Settings

In order to accelerate the acquisition speed of HARDI, the present study uses a 2D Gaussian sampling method to simulate k-space undersampling and a spherical uniform sampling method to simulate q-space undersampling. By using k-q joint sampling, reconstruction experiments with 4-fold acceleration and 8-fold acceleration were performed, that is, simulating 4-fold acceleration (acceleration factor = 4 or AF = 4) by downsampling k-space with a sampling rate of 0.5 and downsampling q-space with a sampling rate of 0.5; simulating 8-fold acceleration (acceleration factor = 8 or AF = 8) by down sampling k-space with a sampling rate of 0.25 and downsampling q-space with a sampling rate of 0.5. After Fourier transform, the k-space data becomes complex, and in the present study, two channels were used to separately train the real part and imaginary part.

Since there have been no reports on the use of deep learning-based k-q space joint undersampling for the fast reconstruction of HARDI, to evaluate the performance of our model, we compared it with the latest k-space signal reconstruction models. The comparison methods simulated AF = 4 and AF = 8 using k-space undersampling rates of 0.25 and 0.125, respectively. The k-space reconstruction models used in the comparison included self-supervised methods SSDU and SSMR [33], and supervised methods Md-Recon-Net, DGDN [34], ISTANet++ [35], and IDPCNN [36].

For the model proposed in the present study, all network layer parameters were initialized using the Kaming uniform method, with a learning rate of 0.0001 and a batch size of 1 for a total of 400 epochs. The comparison models were trained according to their default configurations.

2.7. Quantitative Evaluation Indicators

In order to quantitatively compare the reconstruction results of different methods, we used three objective indicators: root mean square error (RMSE), peak signal-to-noise ratio (PSNR), and structural similarity index (SSIM). Among them, RMSE reflects the root mean square error of the gray level between the reconstructed image I^R and the ground truth image I^G . The smaller the RMSE value, the better the reconstruction quality. It is calculated as follows:

$$RMSE(I^R, I^G) = \sqrt{\frac{1}{hw} \sum_{i=1}^h \sum_{j=1}^w (I_{i,j}^R - I_{i,j}^G)^2} \quad (18)$$

where h and w represent the height and width of the image, respectively.

PSNR reflects the ratio of peak signal energy to average noise energy, and a higher value represents better image quality. It is defined as:

$$PSNR(I^R, I^G) = 10 \log_{10} \left(\frac{\max^2(I^G)}{\frac{1}{hw} \sum_{i=1}^h \sum_{j=1}^w (I_{i,j}^R - I_{i,j}^G)^2} \right) \quad (19)$$

where $\max(I^G)$ represents the maximum gray value of image I^G .

SSIM measures the structural similarity between two images. The closer its value is to 1, the higher the similarity. It is defined by:

$$SSIM(I^R, I^G) = \frac{(2\mu_{I^R}\mu_{I^G} + c_1)(2\sigma_{I^R I^G} + c_2)}{(\mu_{I^R}^2 + \mu_{I^G}^2 + c_1)(\sigma_{I^R}^2 + \sigma_{I^G}^2 + c_2)} \quad (20)$$

where μ_{I^R} and μ_{I^G} represent the grayscale mean values of the reconstructed image and the ground truth image, respectively. σ_{I^R} and σ_{I^G} are the corresponding grayscale variances, while $\sigma_{I^R I^G}$ represents the covariance between the reconstructed image and the ground truth image. c_1 and c_2 are constants.

3. Results

The experiment consisted of two main parts. The first part showcases the training and comparison results of models using HARDI data with denoising preprocessing. In the second part, we present the reconstruction outcomes of noisy HARDI data utilizing the GFT module, along with the reconstruction results of noisy data trained with various denoising preprocessing methods.

3.1. Reconstructing Denoised Data

3.1.1. Reconstruction Results of DWIs

Figure 4 shows the DWIs reconstructed using the proposed model (OAUM) and various comparison models under 4-fold accelerated sampling, along with their respective ground truth (GT) images. For clarity, reconstruction results in two gradient directions are presented in Figure 4, and all results were normalized for consistency. Our method (OAUM) outperforms both self-supervised and supervised methods in terms of image quality improvement in both the gradient directions. Compared to the ground truth full-sampled data, OAUM has the smallest residual error when reconstructing DW images while exhibiting clearer details and textures that can be observed through red arrow areas. IDPCNN and ISTANet++ exhibit poor reconstruction performance at the brain structure edges, while SSDU performs poorly in background regions and skull edges. Although SSMR, MdRecon, and DGDN have acceptable residual ranges, their residual values are still larger than those of our proposed method when compared side-by-side.

Table 1 shows the quantitative evaluation results, which demonstrate that our proposed model achieved superior results. Specifically, it obtained the highest PSNR and SSIM values while also having the lowest RMSE value. Compared to DGDN, a suboptimal method, OAUM reduced the RMSE by 33% and increased the PSNR and SSIM by 8% and 25%, respectively. These findings suggest that DW images reconstructed using OAUM are more accurate representations of real images. In addition, we also show the minimum computational complexity of each model in Table 1. It can be seen that this model has a relatively high minimum computational complexity. It is worth noting that our proposed method reconstructs diffusion-weighted images with 64 gradient directions at the minimum computational complexity, while the compared method only reconstructs diffusion-weighted image with only 1 gradient direction.

Table 1. RMSE, PSNR, and SSIM of DWIs reconstructed from different methods at acceleration factor (AF) = 4 and computational complexity of each model.

Indicator	OAUM	SSDU	SSMR	MdRecon	ISTANet++	DGDN	IDPCNN
RMSE	0.06% ± 0.02%	0.18% ± 0.04%	0.12% ± 0.04%	0.1% ± 0.03%	0.25% ± 0.06%	0.09% ± 0.03%	0.5% ± 0.11%
PSNR	46.1 ± 3.6	36.6 ± 1.1	40.4 ± 1.9	42.1 ± 2.5	33.9 ± 1.5	42.5 ± 2.5	27.8 ± 1.4
SSIM	0.991 ± 0.022	0.944 ± 0.019	0.979 ± 0.004	0.987 ± 0.004	0.915 ± 0.020	0.984 ± 0.021	0.883 ± 0.024
FLOPS	689.5 G	11.9 G	23.6 G	6.8 G	17.7 G	67.4 G	1313.7 G
parameters	0.343 MB	0.323 MB	0.645 MB	0.276 MB	0.725 MB	2.727 MB	7.98 MB

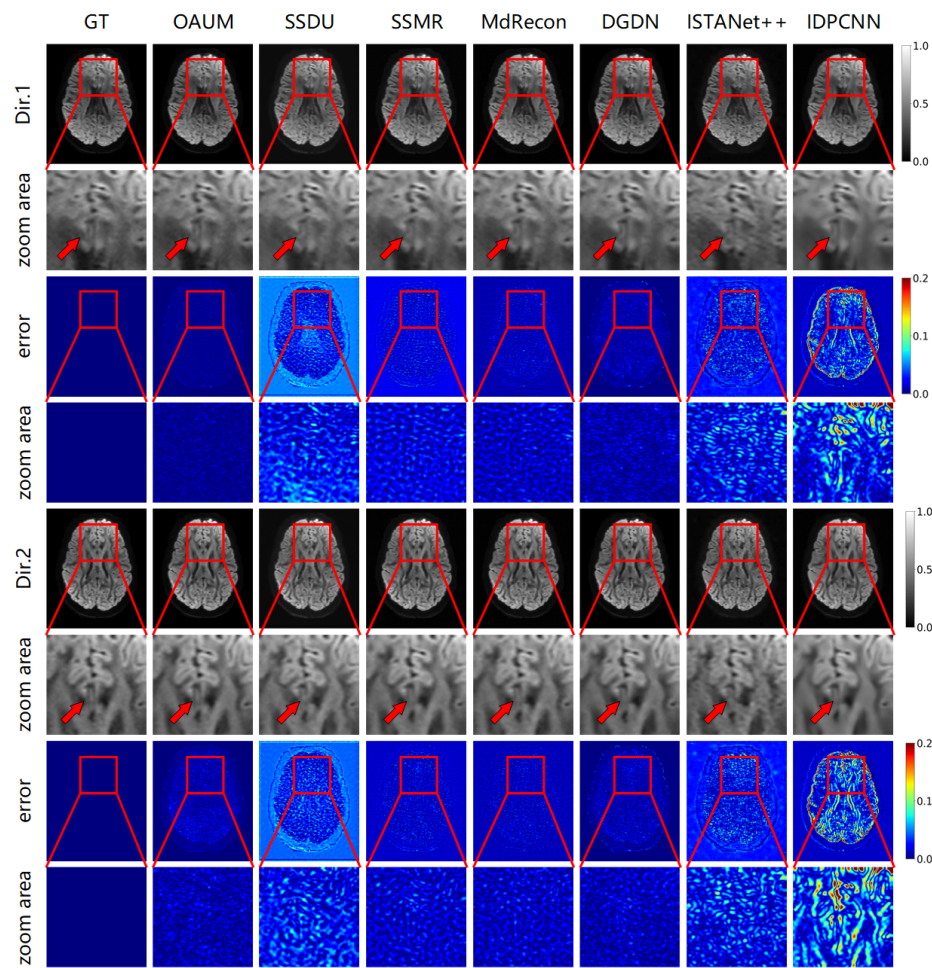


Figure 4. The DWIs reconstructed from models with acceleration factor (AF) = 4 and two diffusion gradient directions.

Figure 5 demonstrates the reconstruction effect of our model at a higher sampling rate. The figure shows the reconstructed DWIs of each model and its residual images compared to the true fully sampled image at an 8-fold acceleration factor (sampling rate of 0.125). Our method outperformed all other methods in detail recovery, as shown by the red arrow in the DW image. Comparing the Dir.1 and Dir.2 directions, OAUM exhibited a worse performance in the Dir.2 gradient direction than the Dir.1 direction because Dir.2 DWIs were reconstructed from q-space undersampled data. However, compared to self-supervised method SSDU and supervised methods ISTANet++ and IDPCNN, OAUM still had significantly lower errors, demonstrating its superiority.

Table 2 gives the quantitative evaluation results for reconstructing DW images using various methods with an 8-fold acceleration factor. The results indicate that our method is superior, while the MdRecon method is inferior under this level of sampling. Our method outperforms the suboptimal approach by achieving an 18% improvement in RMSE and a 5% increase in PSNR.

Table 2. RMSE, PSNR, and SSIM of DWIs reconstructed from different methods at acceleration factor(AF) = 8.

Indicator	OAUM	SSDU	SSMR	MdRecon	ISTANet++	DGDN	IDPCNN
RMSE	0.14% ± 0.04%	0.37% ± 0.08%	0.21% ± 0.05%	0.17% ± 0.05%	0.31% ± 0.07%	0.18% ± 0.05%	0.5% ± 0.11%
PSNR	39.1 ± 2.2	30.4 ± 1.2	35.2 ± 1.8	37.1 ± 2.2	32.0 ± 1.5	36.9 ± 2.1	27.6 ± 1.4
SSIM	0.971 ± 0.021	0.864 ± 0.023	0.950 ± 0.010	0.969 ± 0.010	0.863 ± 0.027	0.963 ± 0.023	0.870 ± 0.034

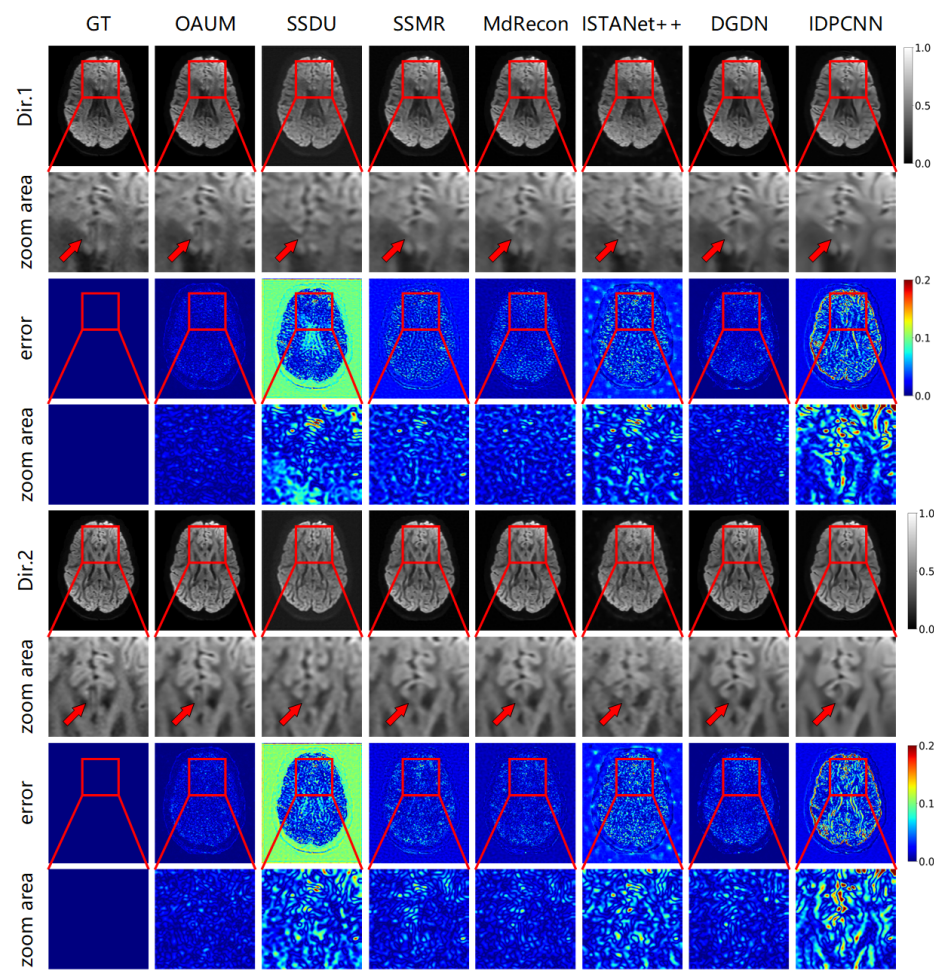


Figure 5. The DWI results reconstructed from models with acceleration factor (AF) = 8 and two diffusion gradient directions.

3.1.2. Fiber Structure and Diffusion Parametric Maps Reconstructed by HARDI

To demonstrate the superiority of our method, we used multidirectional DW images to conduct HARDI reconstruction and calculate fiber orientation (FO) and diffusion parametric maps. Figure 6 shows the fiber orientation maps reconstructed under the 4-fold and 8-fold acceleration factor, along with angle error maps between the primary fiber orientation reconstructed using different methods and the true primary fiber orientation. The OAUM model reconstructs fiber orientations closest to true ones (as shown in white circles in the figure), regardless of whether it is under conditions of 4-fold or 8-fold accelerated sampling, with significantly lower angular errors between true and reconstructed primary fiber orientations than those obtained by comparative methods. The quantitative analysis in Table 3 shows that, under conditions of 4-fold and 8-fold accelerated sampling, compared to the suboptimal model MdRecon, the OAUM model reduced fiber orientation errors by 31% and 17%, respectively.

Table 3. The average angle errors between the real primary fiber orientation and reconstructed primary fiber orientation from different methods at different acceleration factors.

AF	OAUM	SSDU	SSMR	MdRecon	ISTANet++	DGDN	IDPCNN
4	2.2°	4.77°	3.9°	3.55°	6.05°	3.65°	8.91
8	4.62°	7.4°	6.25°	5.94°	7.61°	6.02°	9.7°

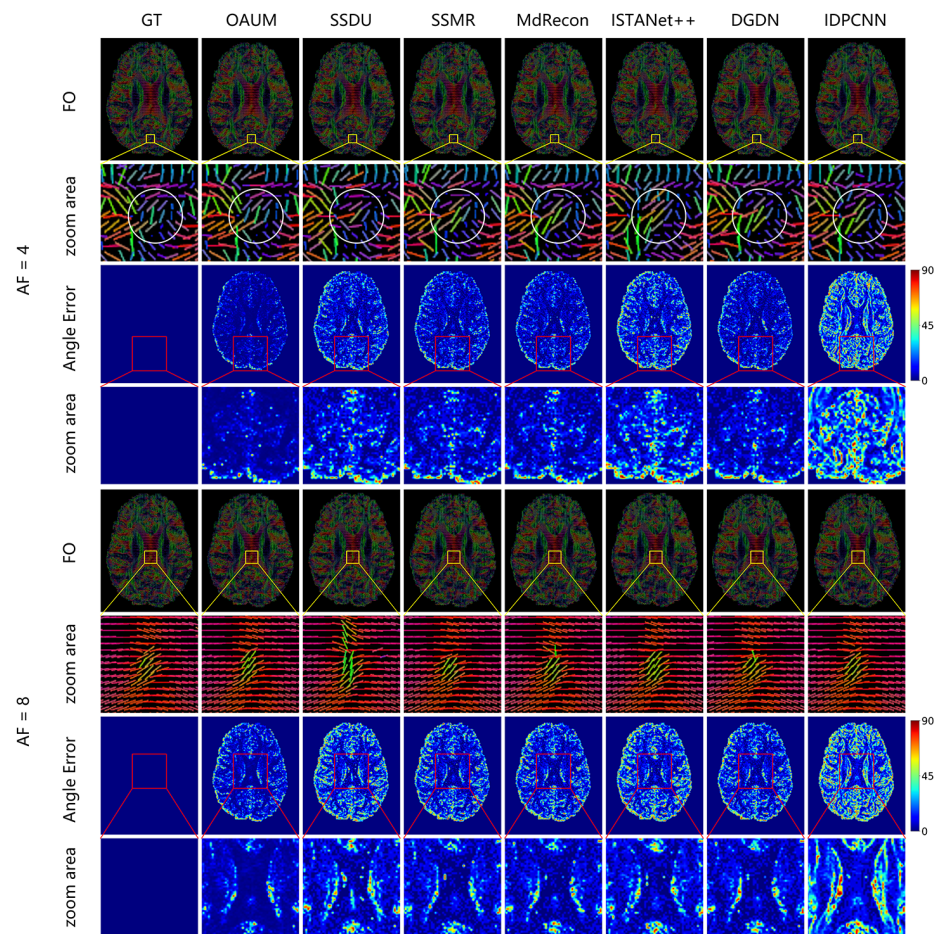


Figure 6. The primary fiber orientations and angle errors estimated from DWIs at different acceleration factors.

Based on the reconstruction of fiber orientation using HARDI, we calculated the generalized fractional anisotropy (GFA) and normalized quantitative anisotropy (NQA) under different acceleration sampling factors to characterize the diffusion of water molecules in tissues, as shown in Figure 7. The given GFA and NQA results, along with corresponding residual maps, indicate that all models except IDPCNN and ISTANet++ can reconstruct diffusion parametric maps well. Our OAUM model had the closest reconstructed GFA and NQA to the real results, with minimal residual values compared to the other models. Although the NQA image reconstructed by DGDN was close to our method, its reconstructed GFA image was slightly worse. Tables 4 and 5 provide quantitative indicators that show that, regardless of whether it is at a 4-fold or 8-fold acceleration factor, the OAUM model obtained optimal quantitative evaluation results for both GFA and NQA, i.e., with the lowest RMSEs and the highest PSNRs and SSIMs. This implies that our proposed strategy ensures accuracy in HARDI parametric maps reconstruction under undersampling conditions.

Table 4. RMSE, PSNR, and SSIM of GFA reconstructed from different methods at different acceleration factors.

AF	Indicator	OAUM	SSDU	SSMR	MdRecon	ISTANet++	DGDN	IDPCNN
4	RMSE	0.014 ± 0.006	0.023 ± 0.006	0.018 ± 0.005	0.015 ± 0.005	0.026 ± 0.006	0.017 ± 0.005	0.039 ± 0.008
	PSNR	37.3 ± 3.0	32.8 ± 2.1	34.8 ± 2.4	36.3 ± 2.7	31.4 ± 2.1	35.5 ± 2.6	27.9 ± 2.0
	SSIM	0.986 ± 0.007	0.975 ± 0.010	0.982 ± 0.009	0.985 ± 0.008	0.959 ± 0.016	0.981 ± 0.009	0.912 ± 0.028
8	RMSE	0.0219 ± 0.008	0.033 ± 0.007	0.025 ± 0.006	0.0224 ± 0.006	0.033 ± 0.007	0.024 ± 0.006	0.043 ± 0.009
	PSNR	33.2 ± 2.6	29.5 ± 2.1	31.8 ± 2.0	32.9 ± 2.3	29.6 ± 2.0	32.2 ± 2.2	27.2 ± 2.1
	SSIM	0.968 ± 0.016	0.942 ± 0.020	0.962 ± 0.015	0.965 ± 0.015	0.942 ± 0.020	0.958 ± 0.017	0.897 ± 0.033

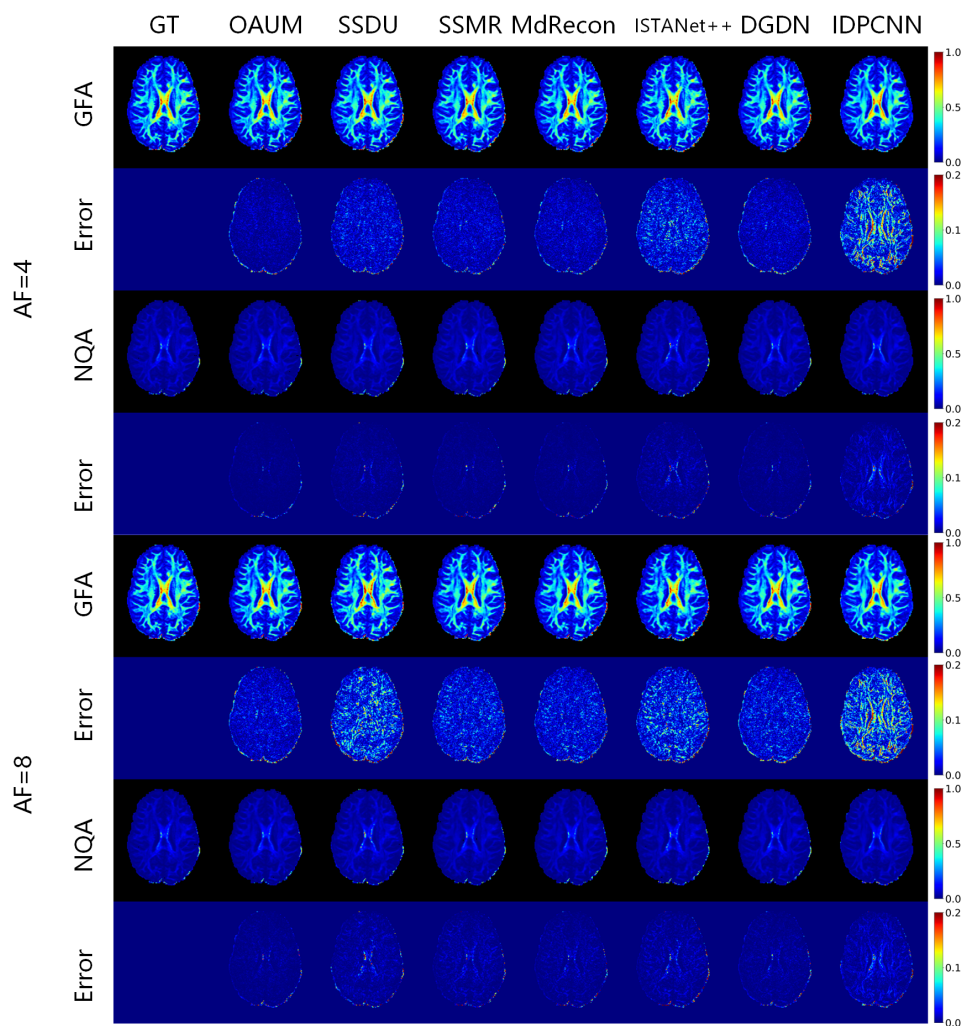


Figure 7. The parametric maps estimated from DWIs at different acceleration factors.

Table 5. RMSE, PSNR, and SSIM of NQA reconstructed from different methods at different acceleration factors.

AF	Indicator	OAUM	SSDU	SSMR	MdRecon	ISTANet++	DGDN	IDPCNN
4	RMSE	0.007 ± 0.002	0.013 ± 0.003	0.010 ± 0.003	0.008 ± 0.002	0.013 ± 0.003	0.008 ± 0.002	0.015 ± 0.004
	PSNR	41.2 ± 2.6	36.1 ± 2.4	38.0 ± 2.6	39.8 ± 2.8	35.5 ± 2.3	39.2 ± 2.3	34.4 ± 2.5
	SSIM	0.986 ± 0.007	0.976 ± 0.008	0.985 ± 0.006	0.986 ± 0.006	0.967 ± 0.011	0.983 ± 0.007	0.944 ± 0.018
8	RMSE	0.010 ± 0.003	0.014 ± 0.004	0.012 ± 0.003	0.011 ± 0.002	0.015 ± 0.004	0.011 ± 0.003	0.017 ± 0.004
	PSNR	37.2 ± 2.3	34.7 ± 2.7	36.9 ± 2.1	37.8 ± 2.0	34.0 ± 2.6	36.6 ± 2.3	33.2 ± 2.4
	SSIM	0.972 ± 0.013	0.957 ± 0.014	0.966 ± 0.011	0.971 ± 0.011	0.957 ± 0.013	0.971 ± 0.011	0.930 ± 0.024

3.1.3. Ablation Experiment

Consistency Constraint for K-Q and Q-K Order Reconstruction

To test the effectiveness of our proposed order-independent reconstruction consistency loss for k-q and q-k reconstruction, we conducted ablation experiments. We trained separate modules for k-space and q-space reconstructions. The k-space module was trained to learn the relationship between full-sampled and undersampled k-spaces using fully sampled data from 32 directions as labels, while the q-space module learned mapping relationships of DW images in different directions with another 32 directions of undersampled k-spaces as labels. Using these trained modules, we compared three methods: sequential reconstruction by k-q order, sequential reconstruction by q-k order, and reconstructed

results with order-independent reconstruction consistency constraint. Figure 8 shows that without order-consistency constraints, the DW image details obtained by other methods were relatively blurry with significant loss (as shown in the zoomed in areas, especially with q-k order), especially at high acceleration rates where their performance was even worse. However, introducing order-independent reconstruction consistency loss greatly improved the DW image quality. By observing diffusion parametric maps reconstructed by different models, it was found that order-independent reconstruction consistency loss helped models obtain better diffusion parametric maps reconstruction results with smaller residual values compared to the true value, which proves the effectiveness of our proposed order-consistency reconstruction idea.

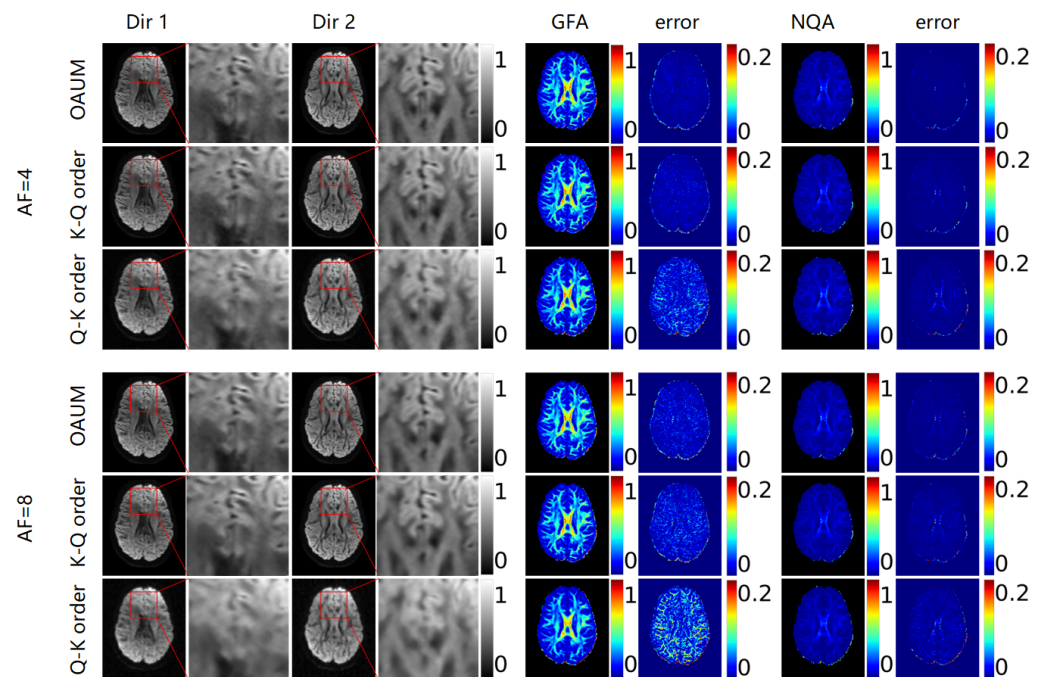


Figure 8. The DWIs reconstructed from OAUM, K-Q order, and Q-K order for ablation at different acceleration factors.

Key Module Ablation for Reconstruction Modules

To enhance the reconstruction effect, we incorporated three modules: the multiscale convolution block (MSCB), K-space flip concatenation module (KFC), and spatial flip concatenation module (SFC) into the OAUM model. We conducted ablation experiments on each module to evaluate the effectiveness, as shown in Figure 9. In the simple OAUM model, ordinary convolution layers were used instead of the MSCB module, and flip and concatenation operations were removed from the KFC and SFC modules. The +MSCB model introduced the MSCB module to the simple OAUM; +MSCB+SFC added the spatial flip concatenation operation to +MSCB; +MSCB+SFC+KFC further included the k-space flip concatenation operation. The results indicate that introducing MSCB can improve DW image and parametric map GFA reconstruction at both 4x and 8x acceleration rates by reducing the RMSE while increasing the PSNR and SSIM. Adding SFC led to an overall improvement in the reconstruction results. However, incorporating KFC improved the performance only at a 4x acceleration rate; at an 8x acceleration rate, there was a slight increase in both DW image's and GFA image's RMSE while the PSNR decreased slightly.

3.2. Reconstructing Noisy Data with GFT

3.2.1. Reconstruction Results of DWIs

Figure 10 shows reconstructed DWIs using various methods with k-q space joint fast reconstruction on input noisy k-space undersampled data under 4-fold and 8-fold

acceleration factors. The figure also includes their corresponding residual maps and zoomed-in maps. For the DN-OAUM method, the denoised result of original noisy DWIs obtained by GFT was used as the reference standard, i.e., the first column in the figure (GT-GFT). To preprocess denoised data for network training, Patch2Self and Neighbor2Neighbor methods were used for OAUM method. GT-P2S and GT-N2N represent data preprocessed using the Patch2Self and Neighbor2Neighbor methods for denoising, respectively, and their corresponding reconstructed DWIs after network training are shown on the right side. Similar to the above figures, two gradient directions' results (Dir.1 and Dir.2) are displayed for each method to reflect both the k-space reconstruction effect and q-space reconstruction effect of networks. Observing the results in the Dir.1 gradient direction first shows that DN-OAUM reconstructed clear and smooth DWIs with very little visual difference from GT-GFT even when zoomed in significantly. However, OAUM trained using GT-P2S data preprocessing contained obvious noise points in its reconstructed DWIs; when observing zoomed-in regions compared to GT-P2S, they cover an additional layer of granular noise while image details became blurred due to the noise influence. Similarly, OAUM trained using GT-N2N also contained noise points in its reconstructed DWIs. Combining error maps revealed that DN-OAUM had minimal reconstruction errors among all methods in the Dir.1 direction with better image quality, while there were significant differences between the OAUM results using different denoising preprocessing techniques.

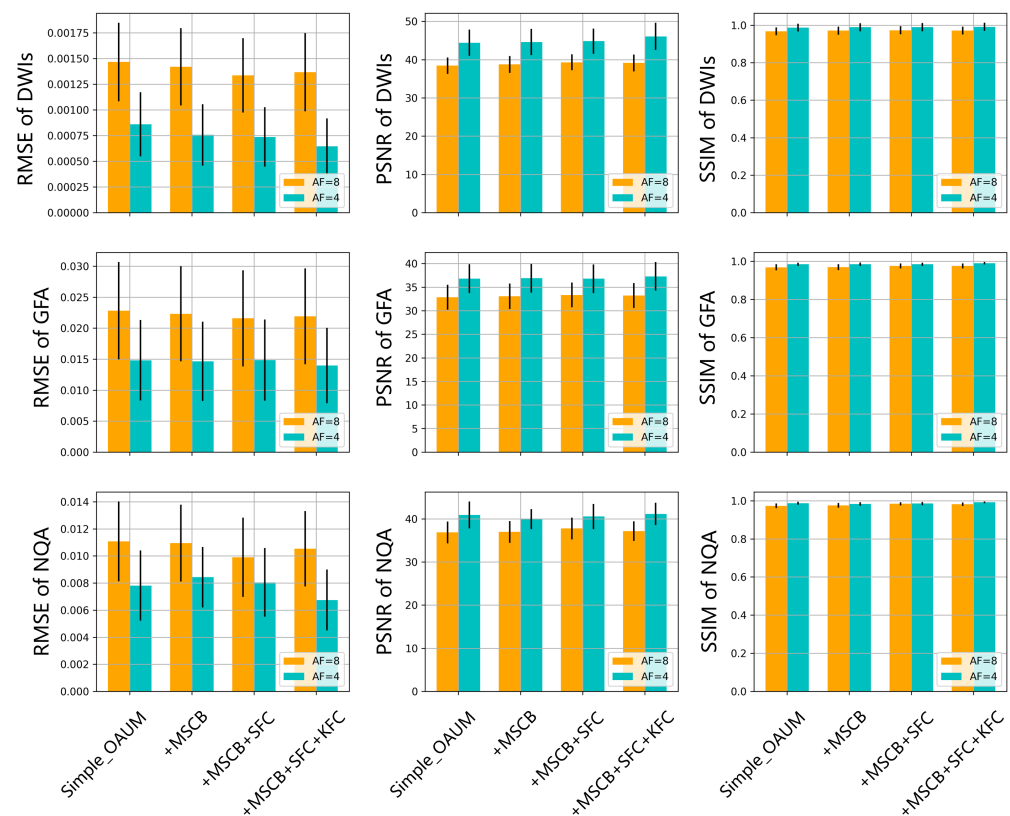


Figure 9. Results of DWI and parametric maps at different acceleration factors.

Upon examining the label data for each method in Figure 10, it is evident that GT-GFT and GT-P2S had fewer instances of visual noise compared to GT-N2N. Consequently, when training OAUM to reconstruct k-space with noisy data using GT-N2N, both the reconstructed result and label contained similar noise, resulting in relatively small errors. However, when using GT-P2S for training OAUM, there was no apparent noise in its label. Nevertheless, upon reconstructing k-space with data affected by noise, its reconstructed result contained a significant amount of noise, which differed significantly from that of GT-P2S. Therefore, this method performs exceptionally well on k-space reconstruction and

can produce high-quality DWIs without significant visual noise compared to GT-GFT while minimizing error.

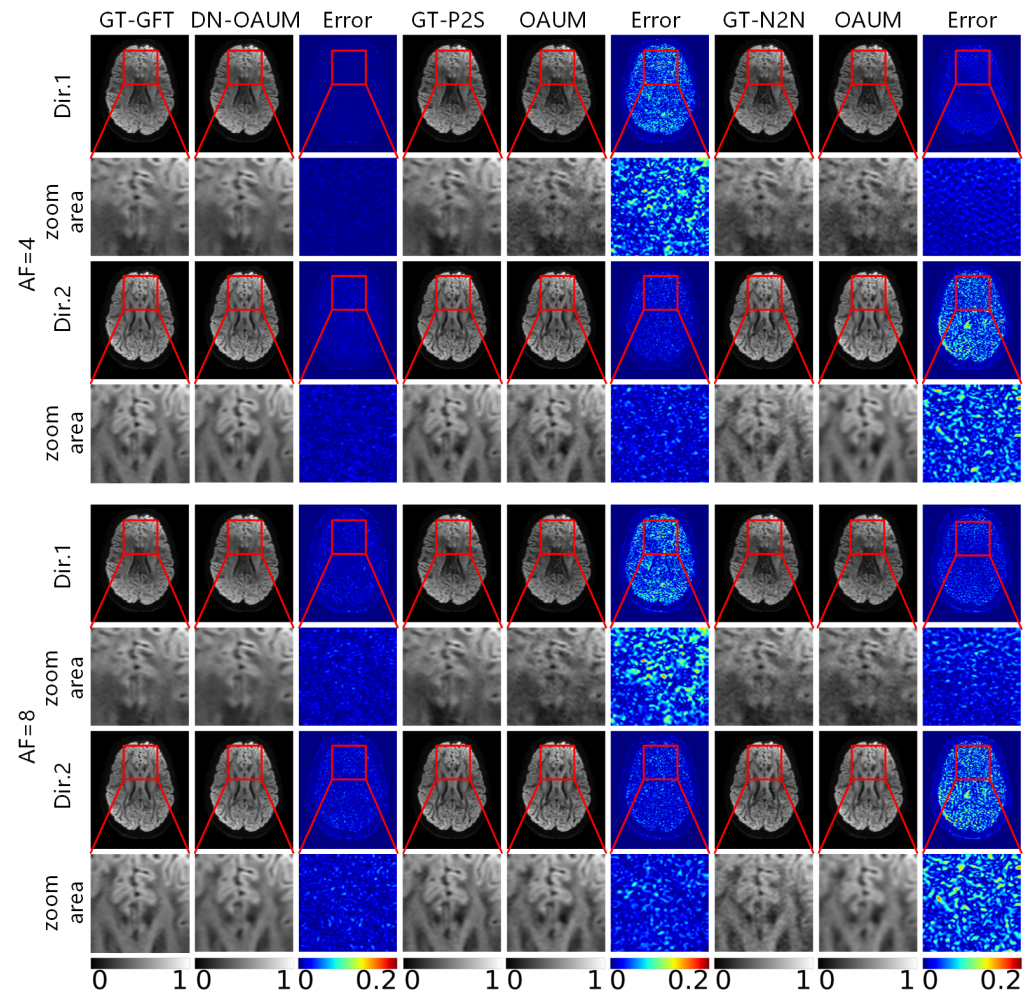


Figure 10. DWIs reconstructed by different methods using noisy data at different acceleration factors.

Upon observing the reconstructed DWIs in the gradient direction of Dir.2, the DN-OAUM method yielded clearly superior image quality. Although visually appealing, the OAUM method trained on GT-P2S data exhibited small particle-like noise when scrutinized under zoomed-in areas. Conversely, OAUM based on GT-N2N data produced blurry DWIs that lacked detail. Error maps corroborate these findings by demonstrating that DN-OAUM’s reconstruction results in the Dir.2 gradient direction were optimal. To better quantify image quality, we conducted a quantitative analysis comparison on reconstructed DWIs as presented in Table 6. The results indicate that the DN-OAUM method outperformed the other comparative methods in terms of quantitative indicators.

Table 6. RMSE, PSNR, and SSIM of DWIs reconstructed from different methods at different acceleration factors.

AF	Indicator	DN-OAUM	OAUM (P2S)	OAUM (N2N)
4	RMSE	0.06% ± 0.03%	0.24% ± 0.09%	0.2% ± 0.12%
	PSNR	46.2 ± 3.7	34.6 ± 3.4	36.7 ± 5.3
	SSIM	0.99 ± 0.003	0.95 ± 0.032	0.94 ± 0.035
8	RMSE	0.12% ± 0.03%	0.25% ± 0.08%	0.25% ± 0.1%
	PSNR	39.4 ± 2.1	34.2 ± 2.8	33.9 ± 3.2
	SSIM	0.971 ± 0.007	0.947 ± 0.029	0.920 ± 0.031

The results of visualizing DWIs reconstructed using various methods under an acceleration factor of 8 are also presented in Figure 10. In the gradient direction Dir.1, the DN-OAUM method showed clear details in the DWIs, while the OAUM method was severely affected by noise. Similarly, for an acceleration factor of 8 in the Dir.2 gradient direction, the DN-OAUM method produced better image quality than the OAUM method. Table 6 provides quantitative results that show a decrease in the RMSE and an improvement in the PSNR and SSIM with the DN-OAUM method compared to the OAUM method.

3.2.2. Fiber Structure and Diffusion Parametric Maps Reconstructed by HARDI

Figure 11 shows a comparison of the reconstructed primary fiber orientation and angle error maps using the above methods. Upon zooming in on the primary fiber orientation map, it becomes apparent that the DN-OAUM method produced results closest to its label under different acceleration factors, while the other methods yielded larger errors. Notably, GT-P2S-trained OAUM exhibited significant errors in fiber orientation reconstruction. The angle error map corroborates these findings and confirms that DN-OAUM is superior in recovering fiber orientation. Table 7 provides further quantitative evaluation results supporting this conclusion.

Table 7. The average angle errors between the real primary fiber orientation and reconstructed primary fiber orientation from different methods at different acceleration factors.

AF	DN-OAUM	OAUM (P2S)	OAUM (N2N)
4	6.2°	11.24°	10.45°
8	8.15°	11.24°	11.03°

The results of the GFA and NQA parameter visualization, calculated from reconstructed HARDI data using the above methods under 4-fold and 8-fold acceleration factors, are presented in Figure 12. Clearly, the DN-OAUM method had smaller errors in both GFA and NQA compared to the two OAUM methods trained with denoising preprocessed data. The latter had larger errors due to noise interference. These findings are supported by quantitative results in Tables 8 and 9, leading to a conclusion that DN-OAUM outperforms OAUM regarding GFA and NQA. Thus, it can be concluded that the denoising effect of the DN-OAUM method is not only effective on DWIs but also has practical significance for diffusion parameter reconstruction.

Table 8. RMSE, PSNR, and SSIM of GFA reconstructed from different methods at different acceleration factors.

AF	Indicator	DN-OAUM	OAUM (P2S)	OAUM (N2N)
4	RMSE	0.024 ± 0.01	0.051 ± 0.01	0.028 ± 0.01
	PSNR	32.9 ± 3.5	25.8 ± 2.6	31.2 ± 2.5
	SSIM	0.978 ± 0.009	0.918 ± 0.032	0.976 ± 0.009
8	RMSE	0.034 ± 0.016	0.040 ± 0.010	0.044 ± 0.014
	PSNR	29.6 ± 3.4	27.8 ± 2.5	27.3 ± 2.6
	SSIM	0.953 ± 0.021	0.938 ± 0.026	0.951 ± 0.017

Table 9. RMSE, PSNR, and SSIM of NQA reconstructed from different methods at different acceleration factors.

AF	Indicator	DN-OAUM	OAUM (P2S)	OAUM (N2N)
4	RMSE	0.013 ± 0.007	0.017 ± 0.004	0.018 ± 0.007
	PSNR	35.05 ± 3.2	31.39 ± 2.9	32.81 ± 2.9
	SSIM	0.945 ± 0.020	0.794 ± 0.065	0.924 ± 0.025
8	RMSE	0.16 ± 0.008	0.015 ± 0.004	0.022 ± 0.009
	PSNR	33.64 ± 3.1	32.06 ± 2.9	30.87 ± 3.0
	SSIM	0.932 ± 0.025	0.809 ± 0.063	0.905 ± 0.029

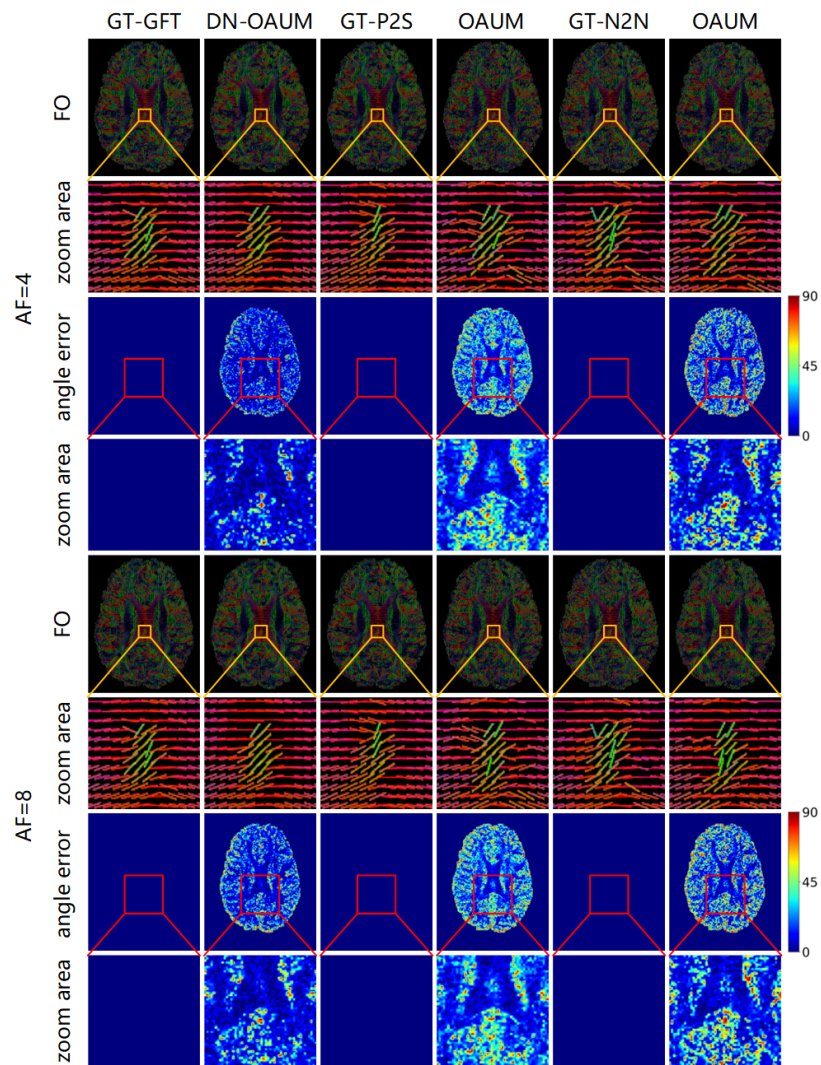


Figure 11. Reconstructed primary fiber orientation maps and angular error maps obtained by each method at different acceleration factors.

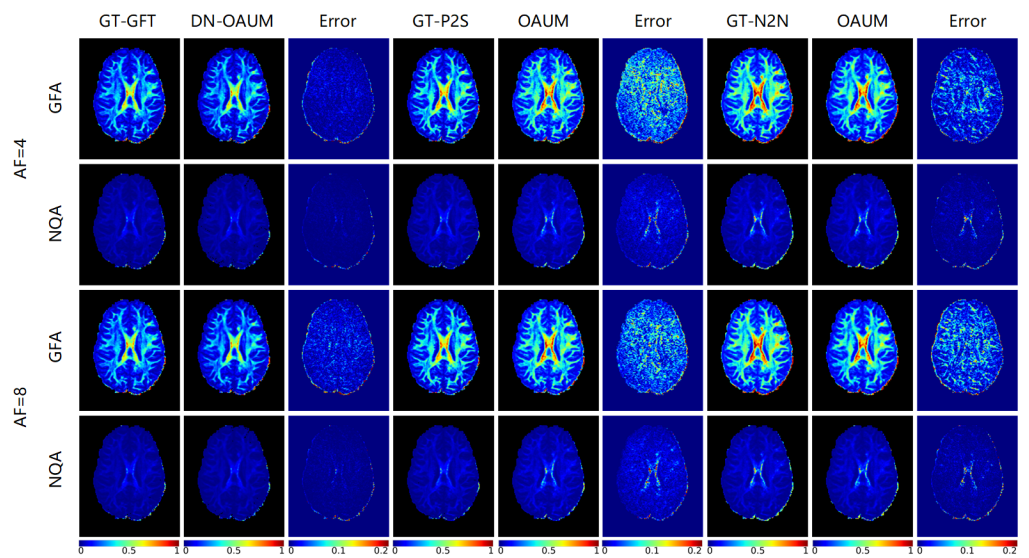


Figure 12. The parametric maps estimated from DWIs at different acceleration factors.

4. Discussion

This work proposes a compressed sensing reconstruction algorithm based on order-consistency and k-q space joint compression. It uses unpaired image data, namely, a set of undersampled k-space data and another set of fully sampled k-space data in different diffusion gradient directions, to reconstruct images from undersampled images with fewer directions to fully sampled images with more directions. In order to reduce the impact of the reconstruction order in k-q joint reconstruction, consistency loss constraints for both k-q and q-k order reconstructions are proposed. In addition, to improve the reconstruction performance, spatial symmetry priors of both k-space and spatial image are utilized, resulting in a k-space flip concatenation module for k-space and a spatial flip concatenation module for spatial information. To evaluate the superiority of this model, we compared it with state-of-the-art compressed sensing-based DWI reconstruction algorithms by means of the HCP public dataset. The experimental results showed that under 4 and 8 acceleration factors, our model can effectively reconstruct detailed information about multidirectional DWIs from undersampled data with fewer directions, which is beneficial for the accurate estimation of complex fiber orientation and diffusion parametric maps in HARDI imaging. Moreover, by introducing the GFT method, the proposed model can quickly and effectively reconstruct noisy data. The introduction of the GFT method can reduce noise interference on reconstruction and further broaden the applicability of OAUM. Through our method, the quality of undersampled HARDI data can be greatly improved, restoring image details and enabling better analysis of images.

Traditional compressed sensing reconstruction algorithms often use iterative approximation methods, resulting in a slow reconstruction speed. The DGDN method splits the traditional approach into two parts: a linear approximation module and a image geometric compensation module. By reconstructing lost texture details through the image geometric compensation module, the traditional method gains learnable ability and alleviates problems such as blur. However, this image geometric compensation module only mines detail information from pixel neighborhoods, which is insufficient for 0.125 sampling rate DW images that lose significant details (as shown in Figure 5) and cannot meet clinical application requirements. To alleviate the instability issue of model reconstruction under multiple sampling rates, ISTANet++ constructs a deep learning model based on the traditional iterative shrinkage threshold algorithm by introducing the sampling rate as conditional information into ISTANet. However, its effectiveness depends on dataset diversity with difficult training leading to unsatisfactory results. Md-Recon-net designs two parallel networks to process k-space frequency domain data and spatial image data using convolutional neural networks that can effectively approximate any bounded function defined on domain and range directly without constructing networks based on traditional methods. Because of its simplicity, it still has visible distortion in reconstructed results (as shown by red arrows in zoomed-in areas of Figures 4 and 5). IDPCNN divides the MRI fast reconstruction problem into two subtasks: denoising and least squares fitting. The denoising task can use any pretrained denoising model, which in a way alleviates the difficulty of obtaining specific data and makes model training more flexible. However, IDPCNN requires pretraining many different levels of denoisers for different rates of downsampling where the number of denoisers significantly affects the reconstruction results with high training difficulty. Although the current best denoisers preserve edge details well, residual maps from Figures 4 and 5 show large errors in the edge details.

SSDU and SSMR are self-supervised learning models that use undersampled data for reconstruction. SSDU divides the original undersampled k-space signal into two parts: using one as input and the other as a reconstruction constraint. This method assigns more low-frequency signals to the input and more high-frequency signals to the output, making it competitive at a $4\times$ acceleration rate. However, there is no constraint on low-frequency parts, such as the background, resulting in large errors in background reconstruction (as shown in Figure 4). At an 8-fold sampling rate, there will be fewer learnable data leading to increased difficulty during model training with significant errors in the reconstructed

results (as shown in Figure 5). Unlike SSDU, SSMR uses two different undersampling templates for the secondary undersampling of raw k-space signals and takes both DW images from these samples as inputs for parallel networks while introducing consistency reconstruction loss. Although its performance at a 4-fold acceleration rate is close to the current state-of-the-art supervised methods, under high-fold subsampling rates, the insufficient signal quantity limits its ability even at an 8-fold acceleration rate like SSDU.

The k-space reconstruction module in the OAUM model, proposed in this paper, differs from the aforementioned models by exploring the relationship between the spatial and frequency domains through transformation. To improve reconstruction quality and the detail recovery effect, we introduced SFC and KFC modules that utilize the prior structural information of data. Additionally, OAUM achieves superior reconstruction quality at an 8-fold acceleration rate through k-q space joint reconstruction and order-consistency constraint. This solves the problem of detail loss observed in comparison methods at an 8-fold sampling rate. Due to the fact that the OAUM method only considers how to train and reconstruct noise-free HARDI data, we further propose the DN-OAUM method, which integrates denoising and reconstruction methods for HARDI data. This enables the fast and high-quality reconstruction of noisy HARDI data.

However, there are still some limitations to this study. Firstly, although the introduction of SFC and KFC in the k-space reconstruction module can improve the reconstruction under a low sampling rate, KFC does not have an advantage under a high sampling rate, implying that different sampling rates have a certain impact on the symmetry prior assumption of k-space. How to design appropriate prior criteria according to different sampling rates is a topic for future research. For example, we could introduce a weight parameter that is used to control the contribution of the KFC module's reconstructed feature map to the final reconstruction result. This weight parameter can be calculated from the sampling rate. Then, in order to ensure consistency between k-q and q-k order reconstructions, we trained two parallel networks for both modules, which resulted in large computational complexity. Finally, since there were no absolute noise-free data as the gold label for this experiment, even though each result of DN-OAUM was optimal, it was not possible to directly prove that DN-OAUM's reconstruction was optimal. The subsequent step should concentrate on enhancing the structures of both the k-space and q-space reconstruction modules. This could be done by minimizing network parameters while simultaneously ensuring high-quality reconstruction. Additionally, efforts will be made to further boost the speed of HARDI reconstruction.

5. Conclusions

The proposed OAUM method successfully utilized nonmatching HARDI data for model training. Compared with existing methods, the proposed method had a better reconstruction quality on noise-free data under different acceleration factors. Therefore, the OAUM method can train and predict models without the need to use fully sampled HARDI data, which, to some extent, alleviates the difficulty of obtaining clinical data. In addition, the proposed DN-OAUM method solved the problem that OAUM cannot reconstruct noisy HARDI data and greatly improved the robustness of the model, making it a potential method for accelerating HARDI data acquisition for clinical applications.

Author Contributions: Conceptualization, Y.G.; methodology, Y.G.; software, Y.G. and Y.C.; validation, Y.G.; writing—original draft preparation, Y.G.; writing—review and editing, Y.C., L.W., Q.C. and Y.Z.; visualization, Y.G. and Y.C. All authors have read and agreed to the published version of the manuscript.

Funding: This research was funded by the National Natural Science Foundation of China (Grant No. 62161004), Guizhou Provincial Science and Technology Projects (QianKeHe ZK [2021] Key 002), the Nature Science Foundation of Guizhou Province (QianKeHe [2020]1Y255), and Guizhou Provincial Science and Technology Projects (QianKeHe ZK [2022] 046).

Data Availability Statement: The dataset used in this article can be found at <https://www.humanconnectome.org> (accessed on 17 May 2023).

Conflicts of Interest: The authors declare no conflict of interest.

Abbreviations

The following abbreviations are used in this manuscript:

dMRI	diffusion magnetic resonance imaging
DWIs	diffusion weighted images
DTI	diffusion tensor image
HARDI	high angular resolution diffusion imaging
SMASH	simultaneous acquisition of spatial harmonics
SENSE	sensitivity encoding
CS	compressed sensing
CNN	convolutional neural networks
ADMM	alternating direction method of multipliers
CRNN	convolutional recurrent neural networks
DAGAN	dealiasing generative adversarial networks
OAUM	order-aware uncertainty minimization
SFC	spatial flip concatenation
KFC	k-space flip concatenation
KDC	k-space data consistency
MSCB	multi-scale convolution module
GFT	graph framelet transform
HCP	human connectome project
AF	acceleration factor
RMSE	root mean square error
PSNR	peak signal-to-noise ratio
SSIM	structural similarity index
GT	ground truth
Dir	direction
FO	fiber orientation
GFA	generalized fractional anisotropy
NQA	normalized quantitative anisotropy

References

1. Sodickson, D.K.; Warren, J.; Manning, J. Simultaneous acquisition of spatial harmonics (SMASH): Fast imaging with radiofrequency coil arrays. *Magn. Reson. Med.* **1997**, *38*, 591–603. [[CrossRef](#)] [[PubMed](#)]
2. Pruessmann, K.P.; Weiger, M.; Scheidegger, M.B.; Boesiger, P. SENSE: Sensitivity encoding for fast MRI. *Magn. Reson. Med.* **1999**, *42*, 952–962. [[CrossRef](#)]
3. Lustig, M.; Donoho, D.L.; John, M.P. Sparse MRI: The application of compressed sensing for rapid MR imaging. *Magn. Reson. Med.* **2007**, *58*, 1182–1195. [[CrossRef](#)] [[PubMed](#)]
4. Lustig, M.; Donoho, D.L.; Santos, J.M.; Pauly, J.M. Sparse MRI: Compressed Sensing MRI. *IEEE Signal Process. Mag.* **2008**, *25*, 72–82. [[CrossRef](#)]
5. Wolfgang, H. Iterative Methods. In *Iterative Solution of Large Sparse Systems of Equations*; Publishing House: New York, USA, 2012; pp. 43–64.
6. Xiaobo, Q.; Weiru, Z.; Di, G.; Congbo, C.; Shuhui, C.; Zhong, C. Iterative thresholding compressed sensing MRI based on contourlet transform. *Inverse Probl. Sci. Eng.* **2010**, *18*, 737–758.
7. Lecun, Y.; Bottou, L.; Bengio, Y.; Haffner, P. Gradient-based learning applied to document recognition. *Proc. IEEE* **1998**, *86*, 2278–2324. [[CrossRef](#)]
8. Chao, D.; Chen, C.L.; Kaiming, H.; Xiaoou, T. Learning a Deep Convolutional Network for Image Super-Resolution. In *Computer Vision—ECCV*; Fleet, D., Fleet, D., Schiele, B., Tuytelaars, T., Eds.; Publishing House: Cham, Switzerland, 2014; pp. 184–199.
9. Kai, Z.; Wangmeng, Z.; Yunjin, C.; Deyu, M.; Lei, Z. Beyond a Gaussian Denoiser: Residual Learning of Deep CNN for Image Denoising. *IEEE Trans. Image Process.* **2017**, *26*, 3142–3155.
10. Zhang, Y.; Li, K.; Li, K.; Wang, L.; Zhong, B.; Fu, Y. Image Super-Resolution Using Very Deep Residual Channel Attention Networks. In *Computer Vision—ECCV*; Ferrari, V., Hebert, M., Sminchisescu, C., Weiss, Y., Eds.; Publishing House: Cham, Switzerland, 2018; pp. 294–310.

11. Yang, Y.; Jian, S.; Huibin, L.; Zongben, X. Deep ADMM-Net for Compressive Sensing MRI. In *Advances in Neural Information Processing Systems*; Lee, D., Sugiyama, M., Luxburg, U., Guyon, I., Garnett, R., Eds.; Publishing House: Barcelona, Spain, 2016.
12. Stephen, B.; Neal, P.; Eric, C.; Borja, P.; Jonathan, E. Distributed Optimization and Statistical Learning via the Alternating Direction Method of Multipliers. *Found. Trends Mach. Learn.* **2011**, *3*, 1–122.
13. Zhang, J.; Ghanem, B. ISTA-Net: Interpretable Optimization-Inspired Deep Network for Image Compressive Sensing. In Proceedings of the 2018 IEEE/CVF Conference on Computer Vision and Pattern Recognition, Salt Lake City, UT, USA, 18–23 June 2018.
14. Beck, A.; Teboulle, M. A Fast Iterative Shrinkage-Thresholding Algorithm for Linear Inverse Problems. *SIAM J. Imaging Sci.* **2009**, *2*, 183–202. [[CrossRef](#)]
15. Qin, C.; Schlemper, J.; Caballero, J.; Price, A.N.; Hajnal, J.V.; Rueckert, D. Convolutional Recurrent Neural Networks for Dynamic MR Image Reconstruction. *IEEE Trans. Med. Imaging* **2019**, *38*, 280–290. [[CrossRef](#)] [[PubMed](#)]
16. Yang, G.; Yu, S.; Dong, H.; Slabaugh, G.; Dragotti, P.L.; Ye, X.; Liu, F.; Arridge, S.; Keegan, J.; Guo, Y.; et al. DAGAN: Deep De-Aliasing Generative Adversarial Networks for Fast Compressed Sensing MRI Reconstruction. *IEEE Trans. Med. Imaging* **2018**, *37*, 1310–1321. [[CrossRef](#)] [[PubMed](#)]
17. Ronneberger, O.; Fischer, P.; Brox, T. U-Net: Convolutional Networks for Biomedical Image Segmentation. In *Medical Image Computing and Computer-Assisted Intervention—MICCAI 2015*; Navab, N., Hornegger, J., Wells, W., Frangi, A., Eds.; Publishing House: Cham, Switzerland, 2015; pp. 234–241.
18. Quan, T.M.; Nguyen-Duc, T.; Jeong, W.-K. Compressed Sensing MRI Reconstruction Using a Generative Adversarial Network With a Cyclic Loss. *IEEE Trans. Med. Imaging* **2018**, *37*, 1488–1497. [[CrossRef](#)] [[PubMed](#)]
19. Eo, T.; Jun, Y.; Kim, T.; Jang, J.; Lee, H.-J.; Hwang, D. KIKI-net: Cross-domain convolutional neural networks for reconstructing undersampled magnetic resonance images. *Magn. Reson. Med.* **2018**, *80*, 2188–2201. [[CrossRef](#)] [[PubMed](#)]
20. Ran, M.; Xia, W.; Huang, Y.; Lu, Z.; Bao, P.; Liu, Y.; Sun, H.; Zhou, J.; Zhang, Y. MD-Recon-Net: A Parallel Dual-Domain Convolutional Neural Network for Compressed Sensing MRI. *IEEE Trans. Radiat. Plasma Med. Sci.* **2021**, *5*, 120–135. [[CrossRef](#)]
21. Koppers, S.; Haarbuerger, C.; Merhof, D. Diffusion MRI Signal Augmentation: From Single Shell to Multi Shell with Deep Learning. In *Computational Diffusion MRI*; Fuster, A., Ghosh, A., Kaden, E., Rath, Y., Reiser, M., Eds.; Publishing House: Cham, Switzerland, 2017; pp. 61–70.
22. Jha, R.R.; Gupta, H.; Pathak, S.K.; Schneider, W.; Kumar, B.R.; Bhavsar, A.; Nigam, A. Enhancing HARDI Reconstruction from Undersampled Data Via Multi-Context and Feature Inter-Dependency GAN, In Proceedings of the 2021 IEEE 18th International Symposium on Biomedical Imaging (ISBI), Nice, France, 2021; 13–16 April 2021.
23. Lyon, M.; Armitage, P. Angular Super-Resolution in Diffusion MRI with a 3D Recurrent Convolutional Autoencoder. In Proceedings of The 5th International Conference on Medical Imaging with Deep Learning, Zurich, Switzerland, 6–8 July 2022; Konukoglu, E., Menze, B., Venkataraman, A., Baumgartner, C., Dou, Q., Albarqouni, S., Eds.; Publishing House: New York, NY, USA, 2022; pp. 834–846.
24. Suyang, L.; Jiliu, Z.; Zhipeng, Y.; Hong, W.; Ying, F. Diffusion MRI super-resolution reconstruction via sub-pixel convolution generative adversarial network. *Magn. Reson. Imaging* **2022**, *88*, 101–107.
25. Vaish, A.; Gupta, A.; Rajwade, A. MSR-Hardi: Accelerated Reconstruction of Hardi Data Using Multiple Sparsity Regularizers. In Proceedings of the 2020 IEEE International Conference on Image Processing (ICIP), Abu Dhabi, United Arab Emirates, 25–28 October 2020.
26. Mani, M.P.; Aggarwal, H.K.; Ghosh, S.; Jacob, M. Model-Based Deep Learning for Reconstruction of Joint k-q Under-Sampled High Resolution Diffusion MRI. In Proceedings of the 2020 IEEE 17th International Symposium on Biomedical Imaging (ISBI), Iowa City, IA, USA, 3–7 April 2020.
27. Yaman, B.; Hosseini, S.A.H.; Moeller, S.; Ellermann, J.; Uğurbil, K.; Akçakaya, M. Self-supervised learning of physics-guided reconstruction neural networks without fully sampled reference data. *Magn. Reson. Med.* **2020**, *84*, 3172–3191. [[CrossRef](#)] [[PubMed](#)]
28. Cole, E.K.; Ong, F.; Vasanaawala, S.S.; Pauly, J.M. Fast Unsupervised MRI Reconstruction Without Fully-Sampled Ground Truth Data Using Generative Adversarial Networks. In Proceedings of the 2020 IEEE International Conference on Image Processing (ICIP), Montreal, QC, Canada, 11–17 October 2021.
29. Dong, B. Sparse representation on graphs by tight wavelet frames and applications. *Appl. Comput. Harmon. Anal.* **2017**, *42*, 452–479. [[CrossRef](#)]
30. Elam, J.S.; Glasser, M.F.; Harms, M.P.; Sotiropoulos, S.N.; Andersson, J.L.; Burgess, G.C.; Curtiss, S.W.; Oostenveld, R.; Larson-Prior, L.J.; Schoffelen, J.; et al. The Human Connectome Project: A retrospective. *NeuroImage* **2021**, *244*, 118543. [[CrossRef](#)] [[PubMed](#)]
31. Fadnavis, S.; Batson, J.; Garyfallidis, E. Patch2Self: Denoising Diffusion MRI with Self-Supervised Learning, In Proceedings of the 34th International Conference on Neural Information Processing Systems, Vancouver, BC, Canada, 6–12 December 2020.
32. Tao, H.; Songjiang, L.; Xu, J.; Huchuan, L.; Jianzhuang, L. Self-supervised Learning for MRI Reconstruction with a Parallel Network Training Framework, In Proceedings of the Medical Image Computing and Computer Assisted Intervention—MICCAI 2021, Virtual, 19–25 June 2021.
33. Hu, C.; Li, C.; Wang, H.; Liu, Q.; Zheng, H.; Wang, S. Neighbor2Neighbor: Self-Supervised Denoising From Single Noisy Images, In Proceedings of the IEEE/CVF Conference on Computer Vision and Pattern Recognition (CVPR), Virtual, 27 September–1 October 2021.

34. Fan, X.; Yang, Y.; Zhang, J. Deep Geometric Distillation Network for Compressive Sensing MRI. In Proceedings of the 2021 IEEE EMBS International Conference on Biomedical and Health Informatics (BHI), Athens, Greece, 27–30 July 2021.
35. You, D.; Xie, J.; Zhang, J. ISTA-NET++: Flexible Deep Unfolding Network for Compressive Sensing. In Proceedings of the 2021 IEEE International Conference on Multimedia and Expo (ICME), Shenzhen, China, 5–9 July 2021.
36. Ruizhi, H.; Fang, L. IDPCNN: Iterative denoising and projecting CNN for MRI reconstruction. *J. Comput. Appl. Math.* **2022**, *406*, 0377–0427.

Disclaimer/Publisher’s Note: The statements, opinions and data contained in all publications are solely those of the individual author(s) and contributor(s) and not of MDPI and/or the editor(s). MDPI and/or the editor(s) disclaim responsibility for any injury to people or property resulting from any ideas, methods, instructions or products referred to in the content.